理學碩士 學位論文

ZnO 나노구조의 형성 및 응용에 관한 연구

A study on the growth and application of ZnO based-nanostructures

2007年 2月

韓國海洋大學校 大學院

應用科學科 半導體物理專攻

鄭 美 娜

理學碩士 學位論文

ZnO 나노구조의 형성 및 응용에 관한 연구

A study on the growth and application of ZnO based-nanostructures

指 導 敎 授

張 志 豪

2007年 2月

韓國海洋大學校 大學院

應用科學科 半導體物理專攻

鄭 美 娜

本 論文을 鄭美娜의 理學碩士 學位論文으로 認准함

위원장　安 亨 秀　(인)
위　원　李 三 寧　(인)
위　원　張 志 豪　(인)

2007 년 2 월

한국해양대학교 대학원

Contents

논 문 요 약

본 논문에서는 II-VI족 화합물 반도체인 ZnO 물질을 나노 구조로 제작하고 그것의 구조적, 광학적, 그리고 Field emitter와 UV laser 같은 나노 소자로서의 응용에 대한 가능성을 고찰하였다. 이 논문의 목적은 성장 조건을 변화시킴에 따라 나노 구조의 모양을 제어하고 최적의 조건에서 얻은 ZnO 나노 구조를 디바이스에 적용함으로써 다양한 반도체 나노 소자로서의 가능성을 보여줌에 있다. 본 논문은 총 6 장으로 구성되어 있으며 각 장의 내용은 다음과 같다.

제 1장에서는 기본적인 ZnO 물성과 나노 구조로 제작됨에 있어서의 특징, 그리고 다양한 응용분야에 대하여 설명을 하였다. 제 2장에서는 제작된 ZnO 나노 구조를 평가하기 위해 본 연구에서 사용한 방법인, SEM, EDX, CL, 그리고 PL 측정에 대하여 정리를 하였다. 제 3장은 성장 온도와 가스 유량을 체계적으로 변화시킴으로서 성장된 ZnO 나노 구조의 형상을 제어함에 있다. 그리고 형상에 따른 ZnO 나노 구조의 구조적, 광학적 특성에 대해 고찰하였다. 제 4장에서는 ZnO 나노 구조의 발광 특성에 대해 설명하였다. 일반적으로 ZnO 내부에 존재하는 Green emission에 대한 원인을 조사하였고, 저온 PL을 측정하여 UV emission의 발광 메커니즘을 알아보았다. 제 5장에서는 제작된 ZnO 나노 구조를 실제 응용을 위한 가능성을 입증하였다. 최적의 조건에서 성장된 ZnO 나노 구조를 이용하여 Field emitter의 전자 방출 소자로서의 시현과, UV 레이저로서의 가능함을 구현

시켰다. 마지막으로 제 6장에서는 본 논문에서 얻은 결과를 정리하여 결론에 대해 기술하였다.

Abstract

In this thesis, synthesis and applications of ZnO materials for the nano-devices such as field emitter and UV laser have been investigated. The objective of this paper is to control the shape of ZnO nanostructures according to the growth temperature and carrier gas fluxes and to show the feasibility for the various nano-devices.

In the chapter 1, the fundamental ZnO properties, characteristics in the nanostructure, and many applications of the ZnO nanostructures are introduced. In the chapter 2, the principles of scanning electron microscope (SEM), energy dispersive x-ray (EDX), cathodoluminescence (CL), and photoluminescence (PL) are explained. In the chapter 3, the control of the shape of ZnO nanostructures is systematically studied by changing the growth temperature and carrier gas fluxes. And the controlled ZnO nanostructures are analyzed in terms of the structural and optical properties. In the chapter 4, the luminescence properties of ZnO nanostructures are investigated including not only the origin the green emission but also the luminescence mechanism of the UV emission. In the chapter 5, the Field emitter device and UV laser operation is demonstrated. Finally, the results found from this thesis are summarized and concluded in the chapter 6.

Chapter 1. Introduction

1.1) Introduction to ZnO compound semiconductor

ZnO has been known as a very important II-VI semiconductor with wide band gap (3.44 eV at 2 K, and 3.37 eV at RT). Also, it has a large exciton binding energy of 60 meV [1], which is more than 3 times larger than those of GaN (23 meV), ZnSe (19 meV) and GaAs (4.2 meV) as listed in Table 1-1. The combination of wide band gap and large exciton binding energy makes ZnO a desirable candidate for a stable room-temperature (RT) ultraviolet (UV) optical device. As well as, ZnO, with a large cohesive energy (1.89 eV), which is comparable to that of GaN (2.24 eV), has good hardness due to the large cohesive energy.

Therefore, it is suitable for UV/ Blue optoelectronic applications such as light-emitting diodes and laser diodes. Recently, ZnO nanostructures as well as ZnO films have received increasing attention due to their potential applications in optoelectronic switches, high-efficiency photonic devices, near-UV lasers and assembling complex three-dimensional nanoscale systems [2-4].

Fig. 1.1 and table 1.1 show the wurzite ZnO structure and the important properties that demonstrate some promising features of ZnO system, respectively.

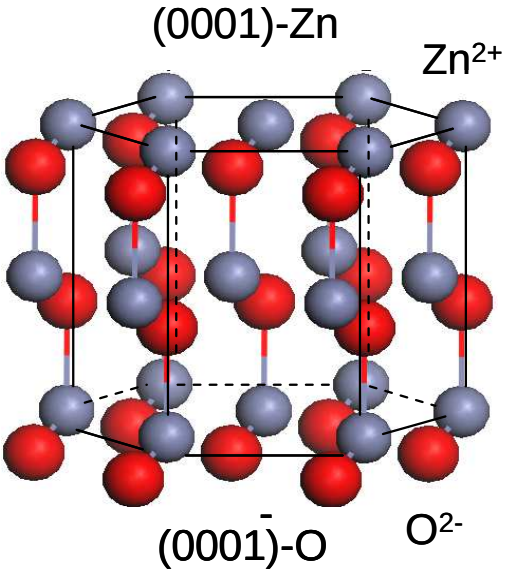

Fig. 1.1 The crystal structure of ZnO wurzite phase

Table 1.1 Comparison of structural and optical properties of ZnO with other materials

material	crystal structure	lattice constant a (Å)	lattice constant c (Å)	cohesive energy E_{coh} (eV)	melting point T_m (K)	band gap (at RT) E_g (eV)	exciton binding energy E_b (meV)
ZnO	Wurzite	3.246	5.207	1.89	2250	3.37	60
ZnS	Wurzite	3.823	6.261	1.59	2103	3.8	29
ZnSe	Zinc blende	5.668	-	1.29	1793	2.70	20
GaN	Wurzite	3.189	5.185	2.24	2791	3.39	21
GaAs	Zinc blende	5.653	-	1.63	1513	1.42	4.9

1.2) ZnO nanostructures

1.2.1) Definition of nanostructure

Nanostructures play an important role in high technology industries. The studies of nanostructures started in the early 1980's and have now become one of the hottest worldwide research fields. Material made with atomic accuracy is called a nanostructured material. Nanomaterials usually show unique properties through nanoscale size confinement, predominance of interfacial phenomena and quantum effect. The size approaches a few to a few hundred nanometers. Many of the outstanding properties are strongly enhanced when the size is smaller than the electron mean-free-path length. Therefore, by reducing the dimension of a structure to nanosize, many inconceivable properties will appear and may lead to different applications.

1.2.2) Quantum size confinement

One of the key factors associated with nanomaterials is the size dependence of their physical and chemical properties. The size of nanoparticles results in spatial confinement of the charge carrier wave functions, which is termed quantum size confinement. With decreasing size, the effective bandgap increases and the relevant absorption and emission spectra shift to bluer wavelengths.

In molecules electrons exist in discrete localized states. In a bulk

semiconductor the large number of molecular orbitals creates a band of continuous electronic states. In the ground electronic states or the valence band (VB), equal numbers of electrons move in forward and reverse directions, resulting in no net conduction, in order to have semiconductors conduct the electrons have to be excited from VB to the bands of excited states or the conduction band (CB). In semiconductors valence and conduction bands are separated by an energy gap, where no Bloch function solutions of the wave equation can exist. The energy gap between the top of the valence band, or highest occupied molecular orbital (HOMO), and the bottom of the conduction band, or lowest unoccupied molecular orbital (LOMO), is called the bandgap. Thermal or photonic excitation can excite electrons to the CB and create holes in the VB. Under this situation, net number of electrons moving in one direction is not canceled out, thus generate net conduction.

The bandgap is of fundamental importance because it determines both the electrical conductivity and the optical absorption onset energy. In a direct bandgap semiconductor the electronic wave functions of the unit cells are in phase,

$$K_c = K_v$$

at the maximum of HOMO and the minimum LUMO energies. In an indirect gap semiconductor, they are out of phase. Analogous to electrical dipole allowed transitions in molecules, a direct band gap semiconductor is

characterized by structured and intense absorption and emission spectra due to allowed electronic transitions.

For nanostructures of semiconductors, quantum confinement effects play an important role of in their electronic and optical properties. The quantum confinement effect can be qualitatively explained using the effective mass approximation [5]. For a spherical particle with radius R, the effective band gap $E_{g\cdot eff}(R)$, is given by:

$$E_{g\cdot eff}(R) = E_g(\infty) + \frac{\hbar^2\pi^2}{2R^2}\left(\frac{1}{m_e} + \frac{1}{m_h}\right) - \frac{1.8e^2}{\varepsilon R}$$

where $E_g(\infty)$ is the bulk band gap, m_e and m_h are the effective masses of the electron and hole, and ε is the bulk optical dielectric constant or relative permittivity. The second term in the right hand side shows that the effective band gap is inversely proportional to R^2 and increases as size decreases. On the other hand, the third term shows that the band gap energy decreases with decreasing R due to the increased coulombic interaction. The second term becomes dominant with small R, thus the effective band gap is expected to increase with decreasing R. The quantum size confinement effect becomes significant especially when the particle size becomes comparable to or smaller than Bohr exciton radius α_B which is given by:

$$\alpha_B = \varepsilon_0\varepsilon_r h2^h / \pi\mu e^2$$

where ε_0 and ε_r are the permittivity of vacuum and relative permittivity of the semiconductor, μ is the reduced mass of the electron and hole, $m_e m_h/(m_e+m_h)$,

and e the electron charge. The Bohr radius of ZnO is around 1.8 nm [6], and particle with radius smaller or comparable to 1.8 nm show strong quantum confinement effects as indicated by a significant blue shift of their optical absorption relative to that of bulk [7].

1.2.3) Application fields of ZnO nanostructures

ZnO, a representative group II-VI compound semiconductor with a direct band gap and large exciton binding energy of 60 meV at room temperature, has attracted considerable attention over the past years owing to its attractive properties, such as good piezoelectric characteristics, thermal stability, and biocompatibility.

Field emission property, as one of the application of nanostructural materials, is of great commercial interest in display and other electronic devices. In the past decade, research on field emission has mainly focused on carbon-base materials, because of their low work function, high mechanical stability, high aspect ratio and high conductivity [8]. With structural properties similar to carbon nanotubes [9], nanostructured ZnO, with the advantage of allowing a relatively high oxygen partial pressure in its applications, should be a good candidate for field emission cathodes.

Another major application for nanostructures is related to the sensing of important molecules, either for medical, environmental, or security-checking

purposes. The extremely high surface-to-volume ratios associated with these nanostructures make their electrical properties extremely sensitive to species adsorbed on surfaces. Researches on the gas sensing of ZnO have attracted great attention for a long time due to their advantageous features, such as higher sensitivity to ambient conditions, lower cost and simplicity in fabrication [10]. It has been found to exhibit sensitivity C_2H_2OH, C_2H_2, CO and other species [11]. The gas-sensing properties of materials are related to the surface state and the morphology of materials.

As previously stated, ZnO is a good candidate for developing high efficiency room temperature excitonic laser due to its a larger exciton binding energy of 60 meV and superiority over nitrides and selenides in thermal stability as well as in resistance to chemical attack and oxidation. Up to now, the room temperature optically pumped UV stimulated emission and lasing have been observed in ZnO thin films [12], ZnO nanowires [13], and signle ZnO nanoneedles [14]. Therefore, ZnO nanostructure is a suitable for UV/blue optoelectronic applications such as light-emitting diodes and laser diodes.

As nanoscale devices, switches are also critical for the important applications like memory and logic devices. Electrical switching on the nanometer and molecular scales has been predominantly achieved through the application of gate potential, as exemplified by nanotube transitors. In fact, several groups have demonstrated that it is possible to create highly sensitive

electrical switches by controlling the photoconductance of individual semiconductor nanostructure [15]. And these highly sensitive photoconducting nanostructure could serve as very sensitive UV-light detectors in many applications for nano-optoelectronics divisions where ON and OFF states can be addressed optically.

1.3) Growth methods for ZnO nanostructure fabrication

1.3.1) Physical vapor deposition (PVD)

The method obtained by condensation from the vapor phase is commonly called physical vapor deposition (PVD). PVD is accomplished through three main steps: generating a vapor phase by evaporation or sublimation of the material in reduced atmosphere; transporting the material from the source to the substrate; and formation of nanostructure by nucleation and diffusion. Examples of PVD include electron-beam evaporation, molecular-beam epitaxy (MBE), thermal evaporation, sputtering, cathodic arc plasma deposition, and pulsed laser deposition (PLD).

When the crystalline size of materials is ≤100 nm, the effects arising from size reduction and increasing amount of interfaces give rise to many interesting and useful properties, as compared to the coarse-grained counterparts. Nanostructure shapes can be fabricated by many methods, but thermal evaporation is a commonly using method as the simplest in the all the

techniques.

For example, solid metal may be evaporated by resistively heating a twisted-wire coil or a metal boat, which contains the metal source. The heat transfer to the metal source is mainly by radiation. The boat temperature is much higher than that of the evaporant in order to efficiently evaporate. For metal sources that react chemically with the holder (boat) materials, induction heating may be used with a ceramic crucible to minimize contamination from the holder (boat). The evaporated atoms or molecules have a vapor pressure P_v, which is proportional to exp ($-\Delta H_v/RT$), where H_v, R, and T are molar latent heat of vaporization, gas constant and temperature, respectively. It is helpful to use ρ_v, to make an order-of-magnitude estimate of the temperature needed for pre-deposition bake-out of vacuum chamber and to determine the type of evaporation source.

1.3.2) Chemical vapor deposition (CVD)

In chemical vapor deposition (CVD), the vaporized precursors are introduced into a CVD reactor, where the precursor molecules adsorb onto a substrate held at an elevated temperature. These adsorbed molecules will be either thermally decomposed or reacted with other gases/vapors to form a solid film in the substrate. Such a gas-solid reaction at the surface of a substrate is called the heterogeneous reaction. Because a number of chemical reactions may

occur in the CVD process, CVD is considered to be a process of potentially great complexity as well as one of great versatility and flexibility. It can be used to grow a variety of materials including metals, semiconductors and ceramics. The solid films can be as amorphous, polycrystalline, or single crystalline materials with the desired properties, depending in the growth conditions. In general, particle formation in the gas phase in a CVD process should be avoided because this will not only considerably deplete the reactants, leading to a non-uniform film thickness, but also incorporate the undesirable particles formation in the gas phase can be used to synthesize nano size powders or particle. Gas-phase nucleation and controlled growth of the particles are of prime concern in the growth processes. The particle-size range is controlled by the number of nuclei formed in the reactor and the concentration of the condensing species.

1.3.3) Sol-gel processing

The sol-gel techniques have been extensively used for the manufacturing of nanophased materials for the last three decades. Among the physical and chemical methods devised for preparation of nanoscaled materials, synthesis from atomic or molecular precursors such as the sol-gel route can give better control of particle size and homogeneity in particle distribution.

The sol-gel processing, which is based on inorganic polymerization reactions, can loosely be defined as the preparation of inorganic oxides such as

glassed and ceramics by wet chemical methods. The goals of sol-gel processing in general are to control the composition homogeneity and the nanostructure during the earliest stages products with nanostructured grains can be attained without vacuum conditions.

The technique exhibits a number of advantages, such as the potentially higher purity and homogeneity and the lower processing temperature, over both conventional ceramic processing and traditional glass melting, especially in preparing multicomponent systems. Many unique processing characteristics of the sol-gel route provide unique opportunities to make pure and well-controlled composition inorganic composited oxides.

This processing can control the structure of a material on a nanometer scale from the earliest stages of processing. This technique to material synthesis is based on some organometallic precursors, and the gels may form by network growth from an array of discrete particles or by formation of an interconnected 3-D network by the simultaneous hydrolysis and polycondensation of organometallic precursors. The size of the sol particles and the cross-linking between the particles depend upon some variable factors such as pH, solution composition, and temperature etc. Thus by controlling the experimental conditions, one can obtain the nanostructured target materials in the form of powder or thin film.

1.3.4) Hydrolysis method

Hydrolysis is attractive because it can produce fine, spherical particles with improved chemical purity, better chemical homogeneity and controlled particle size. Most of the homogeneous precipitation processes involve ionic solutions. Mono-dispersive particles can be prepared by carefully controlling the kinetics particle-forming species, only one burst of nuclei occurs. A continuous diffusion of solutes onto the existing nuclei leads to the growth of the particles. Care must be taken to avoid secondary nucleation to narrow the size distribution.

The easiest way to prepare uniform colloidal metal (hydrous) oxides is based on forced hydrolysis of metal salt solutions. It is well known that most polyvalent cations easily hydrolyze, and that deprotonation of coordinated water molecules is greatly accelerated with increasing temperature. Because hydrolysis products are intermediates to precipitation of metal (hydrous) oxides, these complexes can be generated at the proper rate to eventually yield uniform particles by the adjustment of pH and temperature. In addition, anions other than hydroxide ions can affect the homogenous precipitation of metal ions. These anions can be strongly coordinated to dissolve metal ions or affect the particle morphology without being incorporated in the precipitates.

1.4) Objective and organization of this work

Nanostructures refer to the materials with size dimension on the length scale of a few to a few hundred nanometers. Both equilibrium and dynamic properties of nanomaterials can be very different from those of their corresponding bulk materials or isolated atoms and molecules. Their properties are often strongly dependent on the particle size, shape, and surface properties. For example, spatial confinement is expected to lead the changes in the density of states (DOS) for both electrons and phonons and the rate of electron-hole recombination. The possibility to control the materials properties by varying these parameters is significant to many technological applications ranging from microelectronics to non-linear optics, opto-electronics, catalysis and photoelectrochemistry.

The purpose of this research is focused on the synthesis of pure-ZnO nanostructure growth and its applications to the field emitter or nanolaser. The growth and elucidation of the properties of well-defined nanostructure are needed to understand the fundamental physics of nanostructure, creating nanostructured materials, and developing new applications.

The chapter 2 is an introduction of various measurements, such as scanning electron microscopy (SEM), energy dispersive x-ray spectroscopy (EDX), photoluminescence (PL), and cathodoluminescence (CL), to investigate the grown ZnO nanostructures. To achieve the promising application of ZnO nanomaterial in nanoscale optoelectronic devices, it is important to know its

fundamental properties through many analysis systems.

In this chapter 3, the growth condition of ZnO nanostructure is optimized by different growth conditions, especially for the VI/II ratio by adjusting the growth temperature and carrier gas flux. The structural and optical properties with respect to the shape of different ZnO nanostructures are observed by various measurements.

In chapter 4, the luminescence properties of the ZnO nanostructures are investigated. The origin of the green emission and UV emission, which exist in ZnO material, is defined.

In chapter 5, feasibility of the ZnO nanostructures is examined. From the results of the field emitter device and optically pumping test, we demonstrated the potential application of freestanding tetrapod-type ZnO nanostructures.

In the chapter 6, summary of this thesis and conclusion are given.

References

[1] D.C. Reynolds, D.C. Look, B. Jogai et al, J. Appl. Phys. 88 2152 (2002)

[2] Y.F. Chen, D.M. Bagnall, H. Koh. K. Park et al, J. Appl. Phys 84 3912 (1998)

[3] T. Minami, Mater. Res. Soc. Bull. 25 38 (2000)

[4] M.H. Huang, P. Yang et al, Science 292 1987 (2001)

[5] J. Antony, X.B. Chen, J. Morrison et al, Appl. Phys. Lett. 87 241917 (2005)

[6] Y. Gu, I.L. Kuskovsky et al, Appl. Phys. Lett. 85 3833 (2004)

[7] Y.D. Wang, S. Zhang and X.H. Wu, Eur. J. Inorg. Chem. 727 (2005)

[8] W.A. De Heer, A. Chatelain, and D. Ugarte, Science 270 1179 (1995)

[9] W.B. Choi, D.S. Chung, J.H. Kang et al, Appl. Phys. Lett. 75 3129 (1999)

[10] M.N. Jung, S.Y. Ha, and J.H. Chang, Physica E 31 187 (2006)

[11] C. Xiangfeng, J. Dongli, A.B. Djurisic et al, Chem. Phys. Lett. 410 426 (2005)

[12] Z.K. Tang, M. Kawasaki et al, J. Cryst. Growth 287 169 (2006)

[13] X. Han, G. Wang, and Q. Wang et al, Appl. Phys. Lett. 86 223106 (2005)

[14] H.Y. Yang, S.P. Lau, S.F. Yu et al, Appl. Phys. Lett. 89 011103 (2006)

[15] L. Luo, Y. Zhang et al, Sensors and Actuators A 127 201 (2006)

Chapter 2. Experimental

2.1) General growth mechanisms of nanostructure

2.1.1) Vapor-Solid (VS) growth

The vapor-solid (VS) process is a conventional growth mechanism used for interpreting the growth of nanostructure, such as the growth of nanotetrapods or nanobelts of ZnO, In_2O_3, SnO_2, CdO, Ga_2O_3, and ZnS [1-4]. Most of products were oxides because oxidation seemed to be inevitable due to the inclusion of trace amount of O_2 in the reaction systems. The major advantage of a vapor-phase method is its simplicity and accessibility. In this process, the vapor species are first generated by evaporation, chemical reduction, and other kinds of gaseous reactions. These species are subsequently transported and condensed onto the surface of a solid substrate placed in a zone with temperature lower than that of the source material. With control over the supersaturation factor, one could easily obtain one-dimension (1D) nanostructures.

2.1.2) Vapor-Liquid-Solid (VLS) growth

The vapor-liquid-solid (VLS) is another conventional growth mechanism, which was first proposed by Wanger and Ellis in 1964 for silicon whisker growth [5]. And it was widely used for semiconductor nanowires

preparation, such as Si, GaN, GaAs, InAs, ZnO [6-9]. An important feature of the VLS process is the existence of metal particles that locate at the growth fronts and act as catalytic active sites.

The central idea of VLS growth is the participation of the liquid-forming agents (or so-called catalysts). The catalytic agent is one of important keys to synthesize nanostructure. Another important key is to keep catalytic particles in liquid state during the VLS growth at proper high temperature, which can be chosen by a phase diagram with considering that the melt-point of nano-sized catalytic particles is less than that of bulk materials. For ZnO nanostructures, the growth process can be divided into two stages: the nucleation and the growth of the liquid droplets, and the growth of the nanostructure from the droplets due to supersaturation by the VLS mechanism.

The critical radius of ZnO nuclei with catalyst is given by the equation:

$$r_{\min} = \frac{2\alpha_{LV} V_L}{RTIn_s}$$

where α_{LV} is the liquid-vapor surface free energy, V_L is the molar volume of liquid (droplet), and s is the supersaturating degree of the mixed vapor [10]. Above the equation is shown that thinner Au layers favor the growth of thinner nanowires. By the previous studies, Au clusters with average diameters of 25 nm and 118 nm were obtained after annealing 24 Å 86 Å thick Au films, respectively.

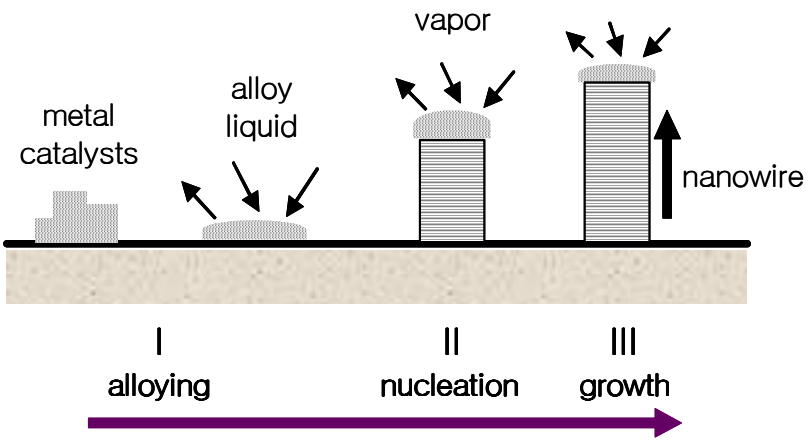

Fig. 2.1 A schematic illustration showing the growth of a nanowire via the vapor-liquild-solid mechanism

2.2) Characterization

2.2.1) Scanning electron microscopy (SEM)

Scanning electron microscopy (SEM) has become one of the most versatile and useful method for direct imaging, characterization, and studying of solid surfaces. As the electrons penetrate the surface, a number of interactions occur that can result in the emission of electrons or photons from (or through) the surface. Appropriate detectors can collect a reasonable fraction of the electrons emitted, and the output can be used to modulate the brightness of a cathode ray tube (CRT) whose x- and y- inputs are driven in synchronism with the x-y voltages rastering the electron beam. In the way an image is produced on the CRT. When the primary electrons collide with atoms of a solid surface in the specimen the electrons take part in various interactions.

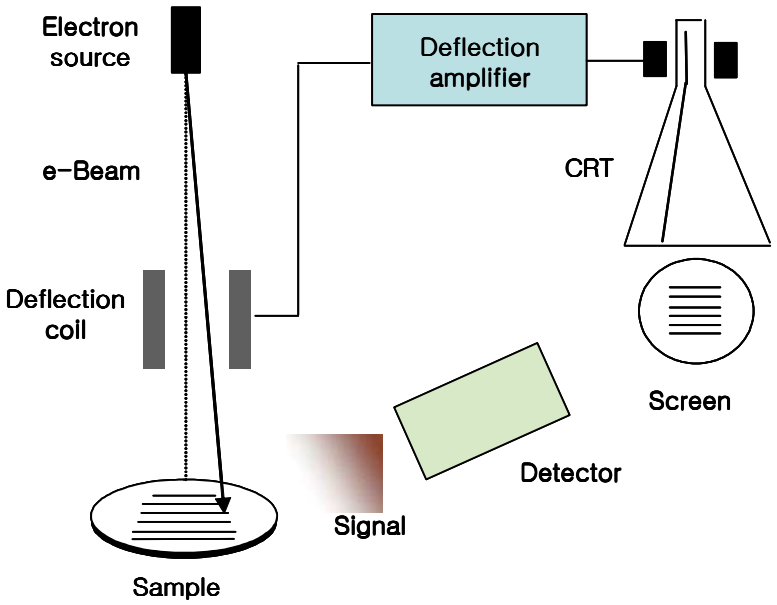

Fig. 2.2 Schematic describing the operation of an SEM

The principle images produced in the SEM are of three types: secondary electron images, backscattering electron images, and elemental X-ray maps. Secondary and backscattering electrons are conventionally separated according to their energies. They are produced by different mechanisms. When a high-energy primary electron interacts with an atom, it undergoes either inelastic scattering with atomic electrons or elastic scattering with the atomic nucleus. In an inelastic collision with an electron, some amount of energy is transferred to the other electron. If the energy transfer is very small, the emitted electron will probably not have enough energy to exit the surface. If the energy transferred exceeds the work function of the material, the emitted electron can

exit the solid. When the energy of the emitted electron is less than about 50 eV, by convention it is referred to as a secondary electron (SE), or simply a secondary. Most of the emitted secondaries are produced much deeper in the material suffer additional inelastic collisions, which lower their energy and trap them in the interior of the solid.

Higher energy electrons are primary electrons that have been scattered without loss of kinetic energy (i.e.,elastically) by the nucleus of an atom, although these collisions may occur after the primary electron has already lost some of its energy to inelastic scattering. Backscattered electrons (BSEs) are considered to be the electrons that exit the specimen with an energy greater then 50 eV, including Auger electrons. However, most BSEs have energies comparable to the energy of the primary beam. The higher the atomic number of a material, the more likely it is that backscattering will occur. Thus a beam passes from a low-Z (atomic number) to a high-Z area, the signal due to backscattering, and consequently the image brightness, will increase. There is a built in contrast caused by elemental differences. It is usual to define the primary beam current i_0, the BSE current i_{BSE}, the SE current i_{SE}, and the sample current transmitted through the specimen to ground i_{SC}, shch that the Kirchoff current law holds:

$$\mathbf{i}_0 = \mathbf{i}_{BSE} + \mathbf{i}_{SE} + \mathbf{i}_{SC}$$

These signals cam be used to form complementary images. As the beam current is increased, each of these currents will also increase. The backscattered electron yield η and the secondary electron yield δ, which refer to the number of backscattered and secondary electrons emitted per incident electron, respectively, are defined by the relationships.

$$\eta = \frac{i_{BSE}}{i_0}, \qquad \delta = \frac{i_{SE}}{i_0}$$

In most currently available SEMs, the energy of the primary electron beam can range from a few hundred eV up to 30 keV. The values of δ and η will change over this range, however, yielding micrographs that may vary in appearance and information content as the energy of the primary beam is changed.

2.2.2) Energy dispersive x-ray spectroscopy (EDX)

Energy-dispersive X-ray spectroscopy (EDX) has been used for quality control and test analysis in many industries including: computers, semiconductors, metals, cement, paper, and polymers. EDX has been used in medicine in the analysis of blood, tissues, bones, and organs; in pollution control, for asbestos identification; in field studies including ore prospecting, archeology, and oceanography; for identification and forgery detection in the fine arts; and for forensic analysis in law enforcement. With a radioactive source, an EDX system is easily portable and can be used in the field more easily than other spectroscopy techniques. The main advantages of EDX are its

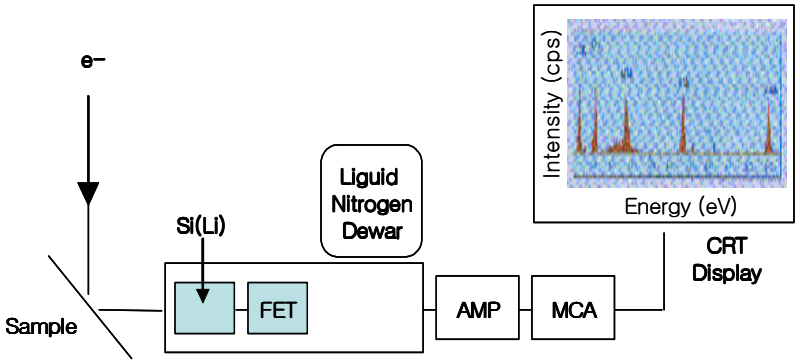

Fig. 2.3 A Schematic of an EDX system on an electron column. The incident electron interacts with the specimen with the emission of X-rays. These X-rays pass through the window protecting the Si(Li) and are absorbed by the detector crystal. The X-ray energy is transferred to the Si(Li) and processed into a digital signal that is displayed as a histogram of number of photons versus energy.

speed of data collection; the detector's efficiency (both analytical and geometrical); the ease of use; its portability; and the relative ease of interfacing to existing equipment.

X-rays are produced as a result of the ionization of an atom by high-energy radiation wherein an inner shell electron is removed. To return the ionized atom to its ground state, an electron from a higher energy outer shell fills the vacant inner shell and, in the process, releases an amount of energy equal to the potential energy difference between the two shells. This excess energy, which is unique for every atomic transition, will be emitted by the atom either as an X-ray photon or will be self-absorbed and emitted as an Auger

electron.

As shown Fig. 2.3, the heart of the EDX is a diode made from a silicon crystal with lithium atoms diffused, of drifted, from and end into the matrix. The lithium atoms are used to compensate the relatively low concentration of grown–in impurity atoms by neutralizing them. In the diffusion process, the central core of the silicon will become intrinsic, but the end away from the lithium will remain p-type and the lithium end will be n-type. The result is a p-i-n diode. When an X-ray photon enters the intrinsic region of the detector through the p-type end, there is a high probability that it will ionize a silicon atom through the photoelectric effect. This results in an X-ray or an Auger electron, which in turn produces a number of electron-hole pairs in the Si (Li). Both charge carriers move freely through the lattice and are drawn to the detector contacts under the action of the applied bias field to produce a signal at the gate of a specially designed field effect transistor mounted directly behind the detector crystal. The transistor forms the input stage of a low-noise charge-sensitive preamplifier located on the detector housing. The output from the preamplifier is fed to the main amplifier, where the signal is finally amplified to a level that can be processed by the analog-to-digital converter (ADC) of the multichannel analyzer (MCA). The height of the amplifier output pulse is proportional to the input preamplifier pulse, and hence is proportional to the X-ray source.

2.2.3) Cathodoluminescence (CL)

Cathodoluminescence (CL) can provide contactless and nondestructive analysis of a wide range of electronic properties of a variety of luminescent materials. The excitation depth can be varied from about 10 nm to several μm for electron-beam energies ranging between about 1 keV and 40 keV.

And it is an optical and electrical phenomenon where a beam of electrons generated by an electron gun (e.g. cathode ray tube) impacts on a phosphor causing it to emit visible light. The most common example is the screen of a television. In geology, a CL is used to examine internal structures of rock samples in order to study the history of the rock. A cathodoluminescence (CL) microscope combines methods from electron and regular (light optical) microscopes. It is designed to study the luminescence characteristics of polished thin

surfaces irritated by an electron beam. To prevent charging of the sample, the surface must be coated with a conductive layer of gold or carbon. CL color and intensity are dependent on the characteristics of the sample and on the working conditions of the microscope. Here, acceleration voltage and beam current of the electron beam are of major importance.

As the result of the interaction between keV electrons and the solid, the incident electron undergoes a successive series of elastic and inelastic scattering events, with the range of the electron penetration being a function of the

electron-beam energy:

$$R_e = \left(\frac{k}{\rho}\right) E_b^a$$

where, E_b is the electron-beam energy, k and α depend on the atomic number of the material and on $E_{b,}$ and ρ is the density of the material. Thus, one can estimate the so called generation (or excitation) volume in the material. The generation factor, i.e., the number of electron-hole pairs generated per incident beam electron, is given by

$$G = E_b(1-\gamma)/E_i$$

where E_i is ionization energy (i.e., the energy required for the formation of an electron-hole pair), and γ represents the fractional electron-beam energy loss due to the backscattered electrons.

In inorganic solids, luminescence spectra can be categorized as intrinsic or extrinsic. Intrinsic luminescence, which appears at elevate temperatures as a near a Gaussian shaped band of energies with its peal at a photon energy

$$h\nu_p \cong E_g$$

is due to recombination of electrons and holes across the fundamental energy gap E_g as shown fig.2.4. Extrinsic luminescence, on the other hand, depends on the presence of impurities and defects. In the analysis of optical properties of inorganic solids it is also important to distinguish between *direct-gap* materials and *indirect-gap* materials. This distinction is based in whether the valence

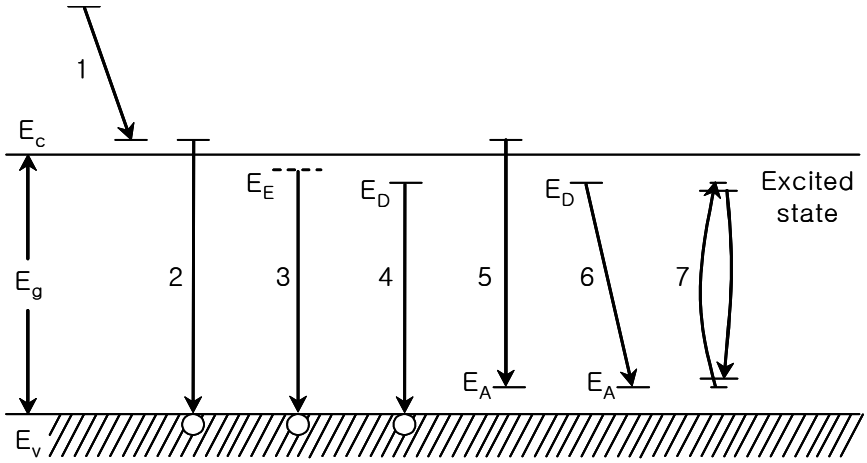

Fig. 2.4 A schematic diagram of luminescence transitions between the conduction band (E_C), the valence band (E_V) and exciton (E_E), doner (E_D), and acceptor (E_A) levels in the luminescent material.

band and conduction band edges occur at the same value of the wave vector k in the energy band E (k) diagram of the particular solid. In the former case, no phonon participation is required during the direct electronic transitions (A phonon is a quantum of lattice vibrations). In the latter case, phonon participation is required to conserve momentum during the indirect electronic transitions; since this requires an extra particle, the probability of such a process occurring is significantly lower than that of direct transitions. Thus, fundamental emission in indirect-gap materials is relatively weak compared with that due to impurities or defects.

A simplified schematic diagram of transitions that lead to luminescence in materials containing impurities is shown in fig.2.4. In process I an electron that has been excited well above the conduction band edge dribbles down, reaching

thermal equilibrium with the lattice. This may result in phonon-assisted photon emission or, more likely, the emission of phonons only. Process 2 produces intrinsic luminescence due to direct recombination between an electron in the conduction band and a hole in the valence band, and thus results in the emission of a photon of energy

$$h\nu \cong E_g$$

Process 3 is the exciton (a bound electron-hole pair) decay observable at low temperature free excitons and excitons bound to an impurity may undergo such transitions. In processes 4, 5, and 6, transitions that start or finish on localized states of impurities (e.g., donors and acceptors) in the gap produce extrinsic luminescence, and these account for most of the processes in many luminescent materials. Process 7 represents the excitation and radiative deexcitation of an impurity with incomplete inner shells, such as a rare earth ion or a transition metal. It should be emphasized that lattice defects, such as dislocations, vacancies, and their complexes with impurity atoms, may also introduce localized levels in the band gap, and their presence may lead to the changes in the recombination rates and mechanisms of excess carriers in luminescence processes.

2.2.4) Photoluminescence (PL)

Photoluminescence is a well-established and widely practiced tool for

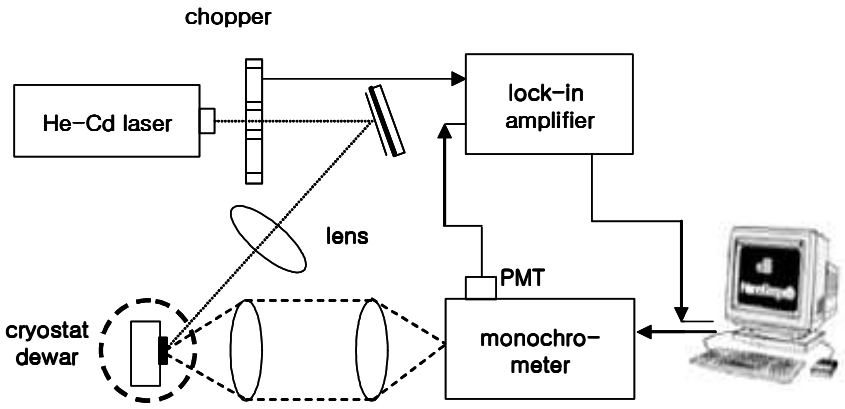

Fig. 2.5 Schematic layout of the photoluminescence system

materials analysis due to its sensitivity, simplicity, and low cost. In the context of surface and microanalysis, PL is applied mostly qualitatively or semiquantitatively to exploit the correlation between the structure and composition of a material system and its electronic state and their lifetimes, and to identify the presence and type of trace chemicals, impurities, and defects. PL systems are largely made up the source of light for excitation (laser), sample holder (or cryostat to measure at low temperature), including optics for focusing the incident light and collecting the luminescence, filter, a double or a triple monochrometer, the optical detector such as photomultiplier tube or CCD or photodiode arrays, and recoding equipments. The experimental setup for the PL measurements used in this study is schematically shown in fig. 2.5.

In PL, a material gains energy by absorbing light at some wavelength by promoting an electron form a low to a higher energy level. This may be

described as making a transition form the ground state to an excited state of a semiconductor crystal (electron-hole creation), The system then undergoes a nonradiative internal relaxation involving interaction with crystalline or molecular vibrational and rotational modes, and the excited electron moves to a more stable excited level, such as the bottom of the conduction band or the lowest vibrational molecular state as shown in the fig 2.6.

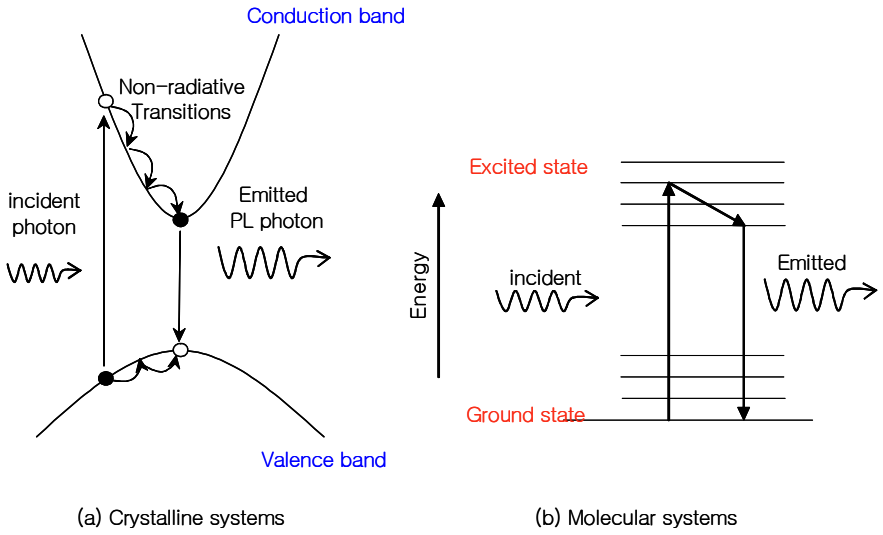

Fig. 2.6 The schematic of PL the standpoint of (a) semiconductor of crystalline system (left) and (b) molecular systems (right)

The major features that appear in a PL spectrum under low excitation are schematically shown in fig.2.7. In order of decreasing energy, the following structures are usually observed: CV, transition from the conduction band to the valence band; X, free exciton; D_0X and A_0X, excitons bound to neutral donors

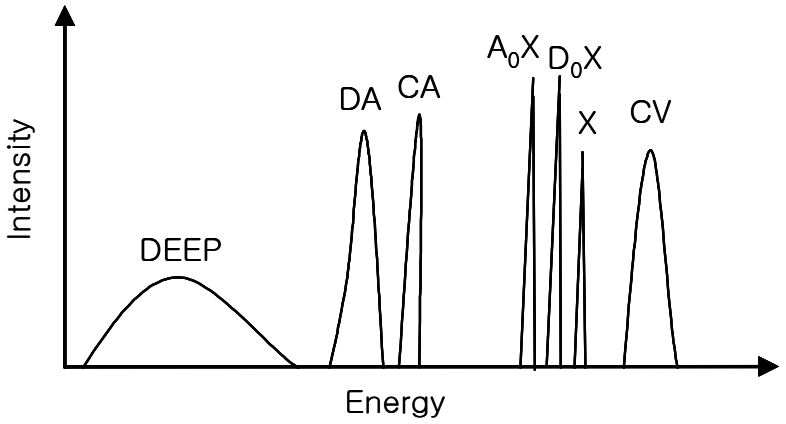

Fig. 2.7 Major features of near band edge photoluminescence spectrum

and acceptors, respectively. DV; transition from a donor to the valence band; CA, transition from the conduction band to an acceptor; DA, transition from a donor to an acceptor; deep, radiative transition at deep states in the forbidden energy gap. All these recombination processes are represented schematically fig.2.8.

The radiative transition from the conduction band to the valence band is usually observed at temperatures higher than the dissociation energy of exciton (~100 K). The line shape is structureless and is given by an effective density of state term multiplied by the Boltzmann filling factor.

$$I_{CV} \propto \sqrt{h\nu - E_g}\,\exp\left(-\frac{h\nu - E_g}{k_B T}\right)$$

E_g is energy gap of the semiconductor, hν is the photon energy of the luminescence and k_BT has its usual meaning. It can be seen from above

equation that the low energy edge of the structure gives the energy gap of the semiconductor and the temperature of carriers can be obtained from the slope of the high-energy part.

Recombination of electrons and holes through free excitons (X) takes place in a high-purity sample at low temperature. Bound excitonic emissions emerge in a near-gap luminescence spectrum as the donor or acceptor concentration is increased from a low level. A prominent type of recombination process involves the annihilation of an exciton bound to either of these species in their neutral charge state.

The recombination process from the conduction band to an acceptor state (CA) is free- to bound transition. As shown in fig. 2.8, the low energy threshold of this CA transition can be described as in above equation for CV transition,

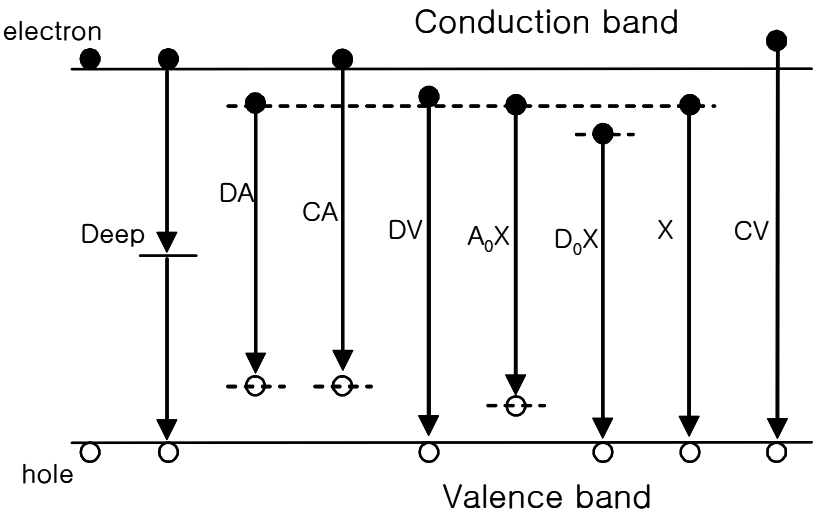

Fig. 2.8 Recombination processes of photoluminescence spectrum

but E_g must be replaced by E_g-E_A, where E_A is the position of energy of the acceptor above the valence band edge. The CA luminescence band is mainly broadened by the kinetic energy of electrons before recombination.

The DA recombination processes compete strongly with the A_0X, and D_0X transitions, especially when the concentrations of donor and acceptor species are increased. The electronic interaction within an ionized donor-acceptor pair after the transitions, as illustrated in fig. 2.8, is responsible for the Coulomb term in the expression for the transition energy.

$$h\nu(DA) = E_g - (E_A + E_D) + \frac{e^2}{\varepsilon r}$$

where e is the elementary charge, r the separation of the donor-accepter pair. The term $e^2/\varepsilon r$ in the above equation is responsible for the spectral dispersion into a very large number of discrete lines. Each line is associated with a different discrete value of r allowed by the lattice structure.

Many impurities and defects give rise to deep energy levels in the forbidden energy gap of semiconductors. These deep states are efficient traps for excess carriers. Not only the capture process but also the resulting recombination through some of the deep centers is nonradiative. The knowledge about the deep level luminescence is important, since it controls the minority carrier lifetime.

References

[1] Y. Zhang, N. Wang, S. Gao et al, Chem. Mater. 14 3564 (2002)

[2] S. Hayashi, H. Saito, J. Cryst. Growth 24/25 345 (1974)

[3] E.G. Wolfe, T.D. Coskren, J. Am, Ceram. Soc. 48 279 (1965)

[4] W-S. Shi, Y-F. Zheng, N. Wang et al, Adv. Mater. 13 591 (2001)

[5] R.S. Wagner, W.C. Ellis, Appl. Phys. Lett. 4 89 (1964)

[6] Y.W. Wang, L.D. Zhang, C.H. Liang et al, Chem. Phys. Lett. 357 314 (2002)

[7] Y.W. Wamg, G..W. Meng, L.D. Zhang et al, Chem. Mater. 14 1773 (2002)

[8] Y.J. Chen, J.B. Li, Y.S. Han et al, J. Cryst. Growth 245 163 (2002)

[9] M.H. Huang, Y. Wu, H. Feick et al, Adv. Mater. 13 113 (2001)

[10] J.T. Hu, T.W. Odom et al, Acc. Chem. Res. 32 435 (1999)

Chapter 3. The shape control of ZnO based nanostructure

3.1) Introduction

ZnO is a semiconductor material with wide direct band gap of 3.44 eV and a large exciton binding energy of 60 meV. Also, the ZnO-based nanostructures are known as an attractive candidate for many application fields. Therefore, numerous studies have been performed on the various ZnO nanostructures such as nanowires, nanorods, tetrapods, nanobelts, nanotubes and nanosheets [1-6]. Among the diverse ZnO nanostructures, tetrapod-shape nanostructures are known as one of the most stable and tough structure, which is an important point for the purpose of application. However, since tetrapod structures have usually diverse mutations such as multipods and second phase structures, structural homogeneity is an important issue. Although, there were several studies about the shape control of ZnO tetrapod-structures, systematical investigation has not been performed yet [7-8]. Therefore, the evaluation of the correlation between the growth conditions and the shapes of nanostructures is important for the successful nano-device applications.

In this chapter, ZnO nanostructures were fabricated by a simple vapor phase transportation method. It was focused on the evaluation of the effects of

two important growth parameters such as growth temperature and VI/II ratio. The structural and optical properties of ZnO nanostructures were characterized by scanning electron microscopy (SEM), energy dispersive X-ray spectroscopy (EDX) and photoluminescence (PL). As a result, the optimum growth conditions for the growth of high quality ZnO tetrapod structure were presented.

3.2) Experimental

ZnO nanostructures were grown on the Si (111) substrates by using a horizontal tube furnace and Zn powder (5N) without any assistance of catalyst. The substrates were cleaned with organic solutions. Dry nitrogen was used as a carrier gas. The flow rate of carrier gas was fixed to 600 sccm, however, various reaction tubes with different diameters (8 mm, 22 mm, 31 mm, 39 mm and 50 mm) were prepared to control the carrier gas flux. Zn source (0.5 g) and Si substrate (5 mm × 5 mm) were placed at the fixed positions, respectively. The growth temperature was controlled from 600 ^{o}C to 900 ^{o}C. The supply ratio (VI/II ratio) of elements was adjusted by the variation of carrier gas flux. The variation of shape and dimension was observed by scanning electron microscopy (SEM) and the chemical composition ratio (O/Zn ratio) of ZnO product was analyzed by energy dispersive X-ray spectroscopy (EDX). The optical properties were characterized by photoluminescence (PL) measurement with He-Cd laser (325 nm, 10 mW) at room temperature.

3.3) Structural characterization of the different ZnO nanostructures

Fig. 3.1 shows SEM images of the typical ZnO nanostructures formed under the various growth conditions. As shown in Fig. 1 (a), under the relatively

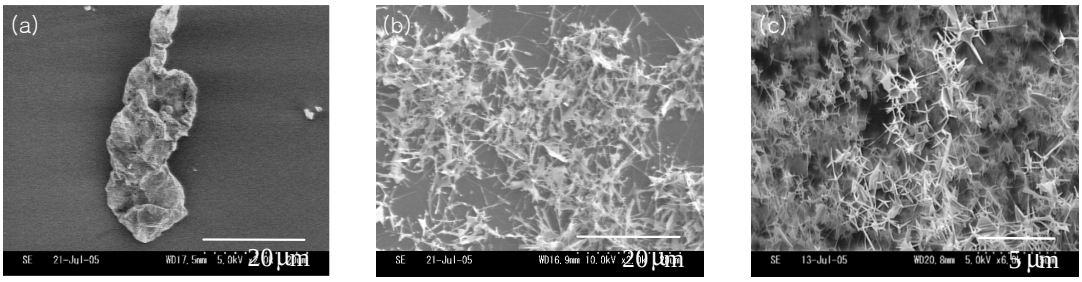

Fig. 3.1 SEM images of the ZnO nanostructures (a) cluster (b) rod (c) tetrapod

low growth temperature (700~800 ^{o}C) and high carrier gas flux ($flux_{gas}$>10 cc/mm^{2}min), clusters with irregular shapes and diverse sizes (5~20 μm) are formed. While, in the intermediate carrier gas flux (1< $flux_{gas}$ <10 cc/mm^{2}min) region, rod or wire types are exhibited as shown in Fig 1 (b). The diameter of typical rod is as large as 100~200 nm with the length of 5 ~ 10 μm. Tetrapods are only obtained at high temperature (800~900 ^{o}C) and low carrier gas flux ($flux_{gas}$<1 cc/mm^{2}min) region.

Tetrapods have considerably uniform shape with 100 nm thick and 1~1.5 μm long legs without second phase growth. Note that when we decrease the growth temperature lower than 600 ^{o}C, only the macro clusters are obtained in all gas fluxes without any proof of nanostructure formation.

In the fig. 3.2, the described results are summarized. Three regions

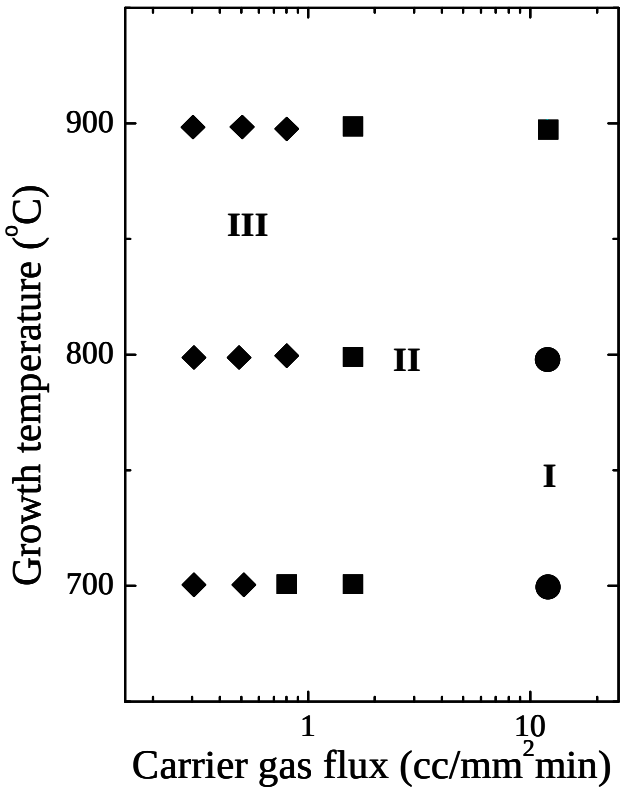

Fig. 3.2 The relationship between the growth conditions and the shapes of nanostructures; the figure divided into three regions based on the shape of nanostructures. Region-I is for cluster-types, region-II is for rod-types and region-III is for tetrapod-type nanostructures.

(from I to III) are divided into the base on the shape of nanostructures. The tetrapod shape is mainly observed from the region-III, which can be characterized by high growth temperature and low carrier gas flux. Within this region, the tetrapods show considerable homogeneity in shape and dimensions. In the region-II, which can be described by the intermediate carrier gas flux, rod- and wire-types are mainly observed. Finally cluster-types are dominated in

the region-I with the highest carrier gas flux and the lowest growth temperature.

From these results, one can find that not only the growth temperature but also carrier gas flux has a great influence on the formation of ZnO nanostructures [9-10]. The growth temperature influences directly the supply of group-II element (Zn) and thermodynamic process of adaptoms on the substrates. Since the carrier gas flux changes the residual pressure of group-VI element (O) in the furnace, the supply ratio (VI/II ratio) will be changed by the variation of carrier gas flux at a given temperature.

P. Yang et al has been synthesized the nanostructures by adjusting the reaction temperature and the partial pressure of oxygen within the system [7]. Diverse tetrapod shapes as well as nanocombs or nanoribbons were found. The exact reason for this subtle change in shape has been not clearly explained so for. But, it could be proposed that the growth rate is deeply correlated to determine the different shape of nanostructure [7-8]. It is well known that the various growth conditions such as temperature, substrate, source material and catalyst have a lot of influence for the determination of the shape and properties of nanostructures [9-16]. For example, the substrate temperature plays an important role for the formation of clusters. Since the Zn and Zn suboxides (ZnO_x, $x < 1$) have low melting temperature (~419 ^oC for Zn) [17], the density of ZnO droplets formed from liquid phase Zn and Zn suboxides will increase as the substrate temperature decreases.

Also clustering is closely related on the thermodynamic conditions. Since, the residual time of adaptoms is a function of substrate temperature, surface energy, and supplying rate of cation/anion, the probability to find clusters would depend on those parameters. Basically, this explanation can be extended to the formation process of the other nanostructures. Also it explains why the shapes of nanostructure have a correlation with the VI/II supply ratio. Moreover, the clusters show high density of oxygen deficiencies in comparison to tetrapods [18], which indicates that not only shape but also chemical composition of nanostructures will be affected by carrier gas flux.

3.4) Composition analysis of the nanostructures

Fig. 3.3 shows the variation of chemical composition of nanostructures. It is plotted in a function of carrier gas flux at the given growth temperatures (700 ^{o}C ~ 900 ^{o}C). The O/Zn ratio, which means the chemical composition ratio of ZnO products, was qualitatively estimated by using EDX measurement. Since the probing depth of electron beam is at least a few μm, the composition should be considered as an average value of whole volume in the focused area. But, we did not perform a quantitative analysis. Because, the exact quantity of Zn and O is not important but only the variation of O/Zn ratio has significance in our experiment.

Although the carrier gas flux decreases by decreasing gas flow or using

large size reaction tube, the VI/II ratio will be increased due to an increment of oxygen supply in the reaction tube, which increases the O/Zn ratio. However, the increase of O/Zn ratio would be saturated at a certain gas flux, when stoichiometric supply is achieved as shown in Fig. 3.3.

The inverted triangle marks show estimated stoichiometric positions at each growth temperature. The VI/II ratio, required for the achievement of stoichiometric composition, increases along with the increase of growth temperature, presumably due to the increase of Zn flux at high temperature. Also more oxygen supply is required at higher temperature, since oxygen re-evaporation will be enhanced.

The above and below parts of the stoichiometric position are nominated as O-rich and Zn-rich regions, respectively. If one compares the results shown in Fig. 3.3 and Fig. 3.2 one can find that under the Zn-rich conditions cluster- and rod-type nanostructures are mainly observed. Furthermore the tetrapods are grown only under the stoichiometric and O-rich conditions, which strongly indicate that the VI/II ratio playsan important role to determine the shape of nanostructures. Since a lot of oxygen deficiencies are prospected from the samples grown under the Zn-rich conditions, oxygen deficiency related deep level emission known as green emission is also expected. Note that, although many studies have performed concerning the origin of green emission from tetrapod structures, there is an obscurity. Nevertheless the similar growth

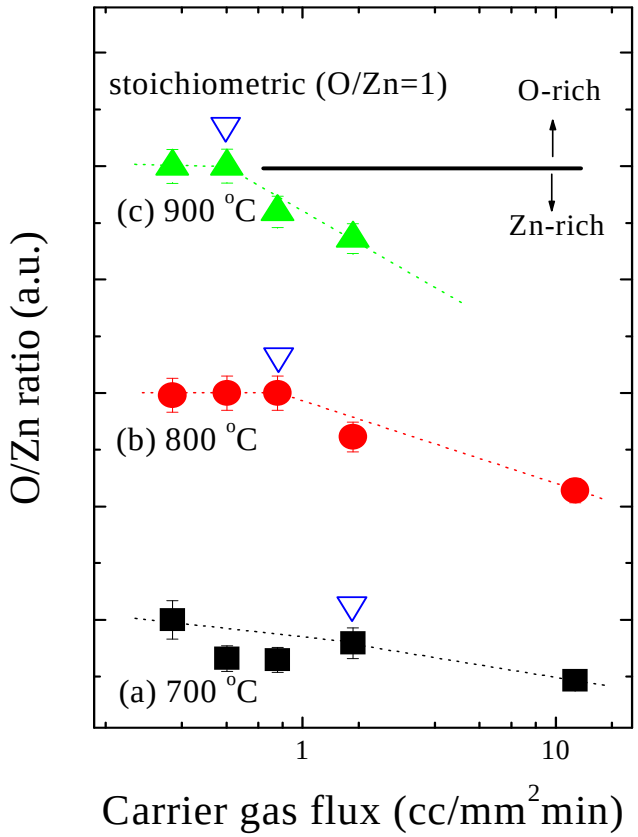

Fig. 3.3 The variation of O/Zn ratio in a function of carrier gas flux at different growth temperature (a) 700 °C (b) 800 °C (c) 900 °C.

conditions such as experimental configuration, temperature and carrier gas, some samples show strong green emission [10,19-20]. while, the other has just negligible deep level emission intensity [20].

On the other hand, in the case of nanorod structures, the green emission intensity shows close relationship with the surface/volume ratio.

It is interesting to note that, in our experiment, the cluster and rod structures are mainly observed under the conditions apt to form oxygen

vacancies (Zn-rich region), while tetrapods are only observed under stoichiometric and O-rich regions. Based on these results, it is considered that the distinction of the green emission between nanorod and tetrapod is mainly originated from the difference of growth conditions for each nanostructure. Because, nanorod structures are grown from liquid phase, the concentration of oxygen vacancies will be easily changed by the growth condition, on the contrary, tetrapods are only obtained under oxygen-rich condition through vapor phase, therefore small variation of the growth conditions will not have large influence on the green emission intensity. From the Fig. 3.2 and Fig. 3.3, 800 ^{o}C is determined as the optimum growth temperature to grow uniform ZnO tetrapods with stoichiometric chemical composition.

3.5) Optical properties

Fig. 3.4 shows room temperature PL spectra of the ZnO nanostructures grown under a variety of growth conditions. Fig. 3.4 (a), grown at 700 ^{o}C and carrier gas flux of 0.8 cc/mm^{2}min, shows the relatively strong deep level emission from 2.8 eV. The observed deep level emission energy is not corresponded to that of well-known green emission (~ 2.4 eV). However, it should be noted that since the growth condition for this sample is in strong oxygen-rich region, additional defects and defect complexes will be easily formed and will make new deep level emission.

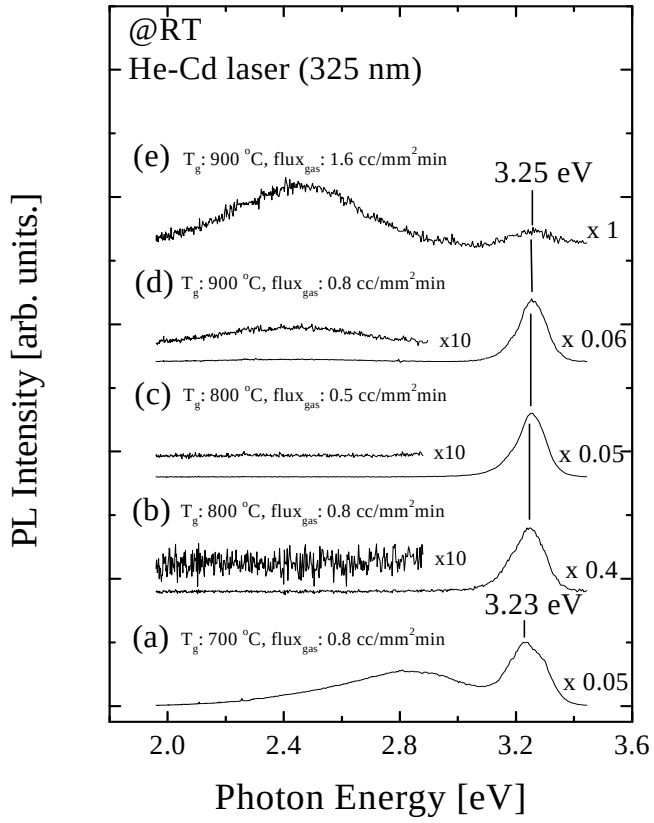

Fig. 3.4 PL spectra of the ZnO nanostructures grown under a variety of growth conditions (a) T_G ; 700 ^oC, $Flux_{gas}$: 0.8 cc/mm^{2}min (b) T_G ; 800 ^oC, $Flux_{gas}$: 0.8 cc/mm^{2}min (c) T_G ; 800 ^oC, $Flux_{gas}$: 0.5 cc/mm^{2}min (d) T_G ; 900 ^oC, $Flux_{gas}$: 0.8 cc/mm^{2}min (e) T_G ; 900 ^oC, $Flux_{gas}$: 1.6 cc/mm^{2}min

Fig. 3.4 (b) and (c) are the PL spectra of samples grown at 800 ^oC under the carrier gas flux of (b) 0.8 cc/mm^{2}min and (c) 0.5 cc/mm^{2}min, respectively. From both spectra negligible deep level emission is observed, which indicates that the growth conditions are suitable for the growth of high quality nanostructure. Fig. 3.4 (d) shows a PL spectrum of the sample grown at 900 ^oC under the carrier gas flux of 0.8 cc/mm^{2}min, which is assigned to Zn-

rich condition. In the PL spectrum, weak green emission is observed. When one increases the carrier gas flux more, the PL spectrum altered as shown in the Fig. 3.4 (e). The green emission dominates the spectrum owing to the increase of oxygen vacancy by the decrease of oxygen supply. Also, this growth condition is not classified into the tetrapod-region, due to the incomplete configuration of nanostructures. The PL spectra, shown in Fig. 3.4, show clearly that the carrier gas flux has a strong correlation with the deep level emission intensity, because it affects the chemical composition of nanostructures formed by changing the oxygen supply.

3.6) Conclusions

ZnO nanostructures were fabricated by vapor transportation method. Growth temperature and carrier gas flux are varied in the wide ranges, and structural, chemical and optical properties are investigated. The VI/II ratio has a large influence on the shape, chemical composition, and optical properties of the nanostructures. Also, it is found that the cluster- and rod-type structures are apt to have oxygen vacancies in comparison with the tetrapods, presumably due to the difference of growth condition and formation process. Finally, based on the distinctions of the chemical composition and configuration of nanostructures, it is argued that the origins of green emission (centered at 2.4 eV) and the blue emission (at 2.8 eV) are different.

References

[1] W.D. Yu, X.M. Li and X.D. Gao, Appl. Phys. Lett. 84 2658 (2004)

[2] W.I. Park, D.H. Kim and S.W. Jung, Appl. Phys. Lett. 80 4232 (2002)

[3] T.W. Kim, T. Kawazoe and T. Sekiguchi, Appl. Phys. Lett. 84 3358 (2004)

[4] Q. Wan, K. Yu and T.H. Wang, Appl. Phys. Lett. 83 2253 (2003)

[5] Y.B. Li, Y. Bando and T. Sato, Appl. Phys. Lett. 81 144 (2002)

[6] L. Dloczik, R. Engelhardt and K. Ernst, Appl. Phys. Lett. 78 3687 (2001)

[7] H. Yan, R. He and J. Pham, Adv. Mater. 15 402 (2003)

[8] J. Zhang, Y. Yang and B. Xu, J. Cryst. Growt, 280 509 (2005)

[9] B.D. Yao, Y.F. Chen and N. Wang, Appl. Phys. Lett. 81 757 (2002)

[10] Z. Chen, N. Wu and Z. Shan, Scripta Mater. 52 63 (2005)

[11] T. Yashi, M. Yasuda and D. Nezaki, Thin Solid films, 464-465 273 (2004)

[12] Y.H. Leung, A.B. Djurisic and J. Gao, Chem. Phys. Lett. 385 155 (2004)

[13] M.H. Huang, Y. Wu and H. Feick, Adv. Mater. 13 113 (2001)

[14] H. T. Ng, J. Li and M. K. Smith, Science, 300 1249 (2003)

[15] S. Y. Li, C. Y. Lee and T. Y. Tseng, J. Cryst. Growth, 247 357 (2003)

[16] S.C. Lyu, Y. Zhang and H. Ruh, Chem. Phys. Lett. 363 134 (2002)

[17] T.B. Massalski, Binary alloy phase diagrams, 2nd ed, 1990

[18] M.N. Jung, S.Y. Ha and S.H. Park, Physica E 31 187 (2006)

[19] V.A.L. Roy, A.B. Djurisic and W.K. Chan, Appl. Phys. Lett. 83 141 (2003)

[20] F. Wang, Z. Ye and D. Ma, J. Cryst. Growth, 274 447 (2005)

Chapter 4. The luminescence of properties of tetrapod ZnO nanostructures

4.1) Introduction

Zinc oxide (ZnO) is a wide-gap (E_g = 3.44 eV) compound semiconductor, which is known as one of the suitable materials for the realization of novel optoelectronic devices, since it has a distinctive optical property such as efficient excitonic emission even at room temperature [1]. Also, ZnO-based nanostructures are expected to reveal novel properties owing to the size effects, which will reduce the density of states at band edges and enhance radiative recombination due to carrier confinement [2]. Therefore, there have been numerous studies on the various ZnO nanostructures such as nanowires [14], nanorods [15], tetrapods [16], nanobelts [17], nanotubes [18], and nanosheets [19] by thermal evaporation [3], vapor deposition [4], hydrothermal method [5], spray pyrolysis [6], catalyst-mediated organization [7-8], and electro-deposition [9]. Among them, vapor transport process with the assistance of catalysts such as Au [10-11], Co [7], Cu [12], NiO [13] is the most popularly selected method. The major advantage of this process is the controllability of the shapes of nanostructures, but the main disadvantage is the remains of the foreign catalysts, which may influence the purity of ZnO

nanostructures [14].

Among the diverse ZnO nanostructures, tetrapod-shape nanostructures are known as stable and tough structure, which is an important point for the purpose of application. Also high purity material could be easily obtained by thermal evaporation without any catalysts or additives. Therefore, there have been several studies on the optical [14, 20-21], structural [21-22], and device applications [17, 23] of this structure. However, it is well known that although strong UV emission is readily observed even at room temperature, one or more peaks in the visible spectral range are unavoidable regardless of the crystal quality of the tetrapods. So far, several mechanisms have been proposed to explain the origin of the visible (green) emission, but it is still ambiguous.

In this chapter, ZnO nanostructures were grown by the simplest method without any assistance of catalysts. The structural and optical properties of ZnO nanostructures were investigated by scanning electron microcopy (SEM), energy dispersive X-ray spectroscopy (EDX), photoluminescence (PL) and cathodoluminescence (CL). The luminescence properties of ZnO nanostructures have been studied focused on the origin of the green emission band.

4.2) Previous studies

4.2.1) Theoretical background on the optical properties

Low-temperature (4-10 K) PL spectra of ZnO typically exhibit the several peaks (label I_0-I_{11}), which corresponds to bound-excitons [24].

However, the assignment of the bound-exciton peaks in ZnO is, in general, controversial for all forms of the samples, ZnO crystal, epitaxy films, and nanostructure. For example, it was proposed that the emission lines I_5 to I_{11} in the lower part of the energy spectrum can be attributed to excitons bound to neutral acceptors. However, other reports in the literature attributed some of these lines to donor bound excitons [24]. The chemical identity of the donors and acceptors responsible for different bound exitons lines still remains unclear.

One of commonly observed bound-exciton lines in ZnO nanostructure is the I_4 line at ~ 3.3628 eV. This emission is typically attributed to the donor bound exciton, and the donor has been identified as hydrogen [24-25]. While in general there is a consensus in assigning the I_4 line to hydrogen donors [24-25], the chemical identity of donors responsible for other donor bound-exciton lines remains unclear.

For acceptor bound-exciton, the most commonly reported peak is located 3.3564 eV. This peak is commonly attributed to excitons bound to Na or Li acceptors [26]. Alkali metals are predicted to produce shallow acceptors on the cation site, but the experimental results demonstrate that doping with group 1 ions produces complex results. Other acceptor levels have also been proposed, such as an acceptor complex involving the N impurity in an O site [27].

However, some authors attribute this line to a donor bound-exciton instead [24]. Therefore, further work is needed for conclusive identification of the origin of different bound-exciton lines in ZnO. The assignment of several bound exciton lines, especially I_9, is still controversial and conclusive chemical identification of the majority of donors and acceptors has not been accomplished.

Low-temperature PL spectra can also contain donor-acceptor pair transitions and longitudinal optical (LO) phonon replicas [28]. First-, second-, and third- order LO phonon replicas can typically be observed. The LO phonon energy can be determined from the separation between the exciton peaks and their LO phonon replicas, and for ZnO it is 71-73 meV in the spectral region (3.218-3.223 eV).

Biexciton emission was observed at 77 K in high-quality epitaxy ZnO films. The biexciton binding energy was estimated to be 15 meV [29]. Biexciton emission has also been observed in ZnO nanowires and nanorods. Clear observation of free-exciton and biexciton lines at low temperature is usually considered as an indication of very good sample quality.

4.2.2) UV emission of in terms of different ZnO nanostructures

In room-temperature PL spectra, some variation of the position of the PL peak can be observed for different nanostructures. Different UV peak position (387 nm for tetrapods, 381 nm for needles, 397 nm for nanorods, 377

nm for shells, 379 nm for faced rods, 385.5 nm for ribbons/combs) can be observed. Individual nanostructures, such as nanobelts, exhibited UV emission in a range between 384 nm and 391 nm. These differences in the peak positions of individual nanostructures indicate that there is likely a different explanation for the variation in the band-edge emission in ZnO nanostructures reported in different studies.

4.2.3) Defect emissions

Room-temperature PL spectra from ZnO can exhibit a number of different peaks in the visible spectral region, which have been attributed to the defect emission. Emission lines at 405, 420, 446, 485, 510, 544, 583, and 640 nm have been reported.

Green emission is the most commonly observed defect emission in ZnO nanostructures, similar to other forms of ZnO. It is often attributed to singly ionized oxygen vacancies, antisite oxygen, oxygen vacancies, zinc interstitials, and Cu impurities. Therefore, the origin of the green emission is still an open and controversial question.

Yellow defect emission is also commonly reported in ZnO nanostructures. This emission is typically attributed to oxygen interstitial, although a Li impurity represents another possible candidate [30]. The deep levels responsible for green and yellow emissions were found to be different,

unlike the defect responsible for the green emission, the defect responsible for the yellow emission is not located at the surface [30]. In addition to green and yellow emissions, orange-red emissions are often also observed. The visible emissions at ~ 540 nm and 610 nm in ZnO dendritic were attributed to surface dislocations [31]. Orange-red emission at ~ 626 nm in ZnO nanorods was attributed to oxygen interstitials. In addition, orange emission at 640-650 nm in ZnO needles and nanowires was proposed to be oxygen-rich samples on agreement with a previous study on ZnO films.

4.3) Experimental

ZnO nanostructures were prepared by using three-zone horizontal tube furnace without the assistance of catalyst. Before the growth, the reaction tube was baked at high temperature for 1 hr to eliminate residual contaminations. Pure Zn powder (4N) was used as a source material. And it was placed at the highest temperature zone (~ 900 ^{o}C) using a quartz boat. Then, the substrates were located in the designated position of different temperature from 450 to 600 ^{o}C in the same reaction tube No carrier gas was used but the reaction furnace was pumped out from the end of low temperature side with the pumping rate of 24 liter/min. The pressure in the reaction furnace, measured at the outlet of the furnace, was 3×10^{-1} Torr during the growth. It is assumed that both Zn and O supplying rate are kept constant for all samples. After 30 minutes growth, the

samples were characterized by scanning electron microscopy (SEM), energy dispersive x-ray analysis (EDX), photoluminescence (PL) and cathodoluminescence (CL).

4.4) Structural evaluation

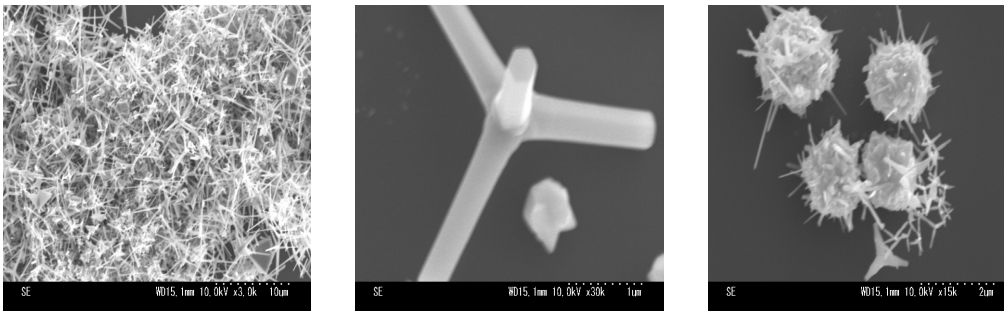

(a) (b) (c)

Fig. 4.1 SEM images of ZnO nanostructures (a) ZnO tetrapods (Ts = 600 ^{o}C) (b) typical shape of ZnO tetrapods (c) ZnO clusters (Ts = 450 ^{o}C)

Fig. 4.1 shows SEM images of ZnO nanostructures. High-density ZnO tetrapod structures with hexagonal legs and clusters with arbitrary shapes are obtained. Considerable variation of the shape of tetrapods is not observed in our samples. As shown in Fig. 4.1 (a), the typical diameter and length of tetrapods are about 100 ~ 200 nm and 3 ~ 5 μm, respectively. However, the density of tetrapods decreases as the substrate temperature decreases. In contrast, significant influence of the growth temperature is observed from the

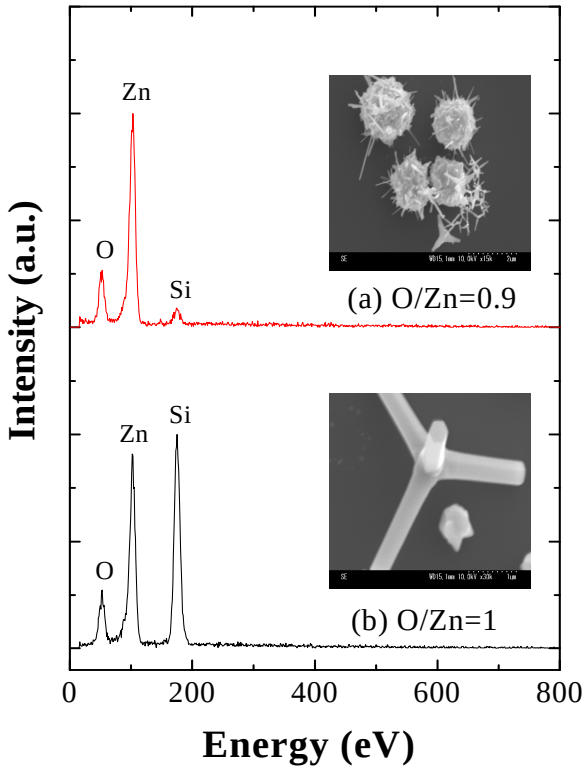

Fig. 4.2 EDX spectra of ZnO tetrapods and clusters (a) Clusters have a lot of oxygen deficiencies, while (b) tetrapods show stoichiometric composition.

ZnO clusters. With decreasing substrate temperature, the density and size of ZnO clusters increase. Fig. 4.1 (c) shows a cluster formed at 450 ^{o}C with large diameter of 1.5 ~ 2 μm and 0.4 ~ 1 μm long needle-like shapes on the surface.

Although, it is well known that various growth conditions such as growth temperature [3-4], growth time [15], substrate [32], source [33] and catalyst [7, 10-11, 12-13] have strong influence on the shape and quality of nanostructures, the growth mechanism of ZnO nanostructures still has many obscurities. However, it is clear that the growth temperature plays an important

role for the formation of clusters. Since the Zn and Zn-suboxides (ZnO_x, $x < 1$) have low melting temperature (~419 ^oC) [34], if one assumes constant supply rate of Zn and Zn-suboxides, the density of ZnO droplets formed from liquid phase Zn and Zn-suboxides will increase as the substrate temperature decreases.

4.5) Composition analysis of ZnO nanotetrapods

Fig. 4.2 shows EDX spectra of ZnO tetrapods and clusters. The atomic composition of ZnO tetrapods is found to be very close to the stoichiometric one (1_{Zn}: 1_O). But, ZnO clusters show considerable oxygen deficiencies (1_{Zn}: 0.9_O). The origin of O deficiency in the ZnO clusters can be explained in terms of the vapor-liquid-solid (VLS) growth mechanism. Zn would be transported in gas phase such as Zn (g) or ZnO_x (g, $x<1$), thus Zn (g) or ZnO_x (g, $x<1$) will be deposited on substrate. Also it is valid during the initial nucleation of nano-particles. If the ambient temperature is above the melting temperature of Zn and Zn-suboxides, the deposited Zn will undergo phase change to Zn (*l*) or ZnO_x (*l*) ($x<1$). Those will be segregated into the nuclei [19]. Thus the clusters and initial nuclei tend to have oxygen deficiencies. While, the formation mechanism of ZnO tetrapods have not been definitely explained so far. Generally, it is known that ZnO tetrapod are formed by the vapor-solid (VS) mechanism [35], which is the oxidation process of evaporated Zn (g). A previous report [37] indicates that the supply rate of oxygen determines the length and shape of tetrapod. In our

case, therefore, constant oxygen supply rate due to high pumping rate is presumably responsible for the uniform size of the tetrapods.

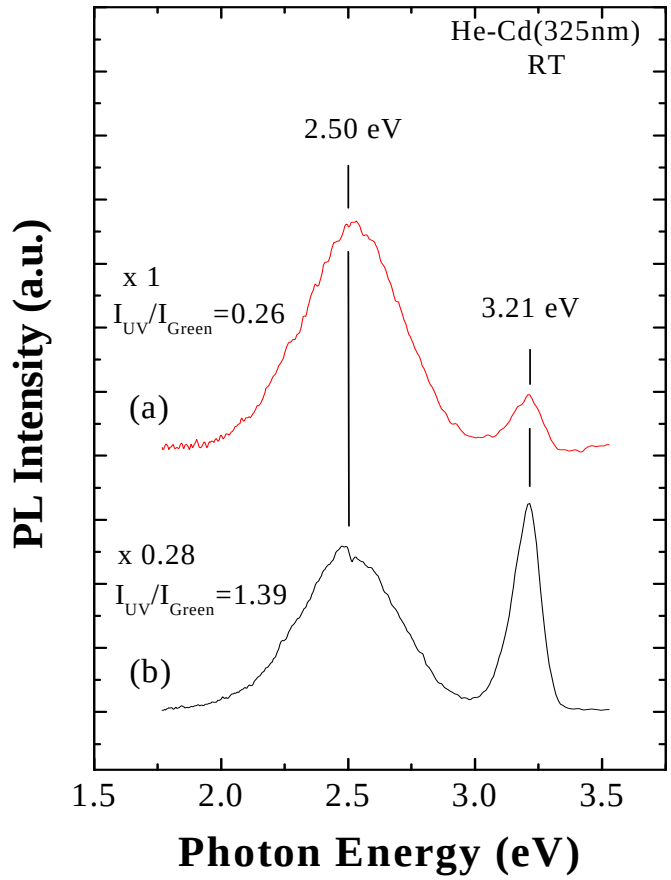

Fig. 4.3 Room-temperature PL spectra. UV emission at 3.21 eV and green emission at 2.5 eV are observed. PL spectra of the samples grown at (a) 450 ^{o}C and (b) 600 ^{o}C

4.6) Optical evaluation of ZnO nanotetrapods

Fig. 4.3 shows PL spectrum measured at room temperature using 325 nm line of a He-Cd laser with the excitation power of 20 mW. As reported in

the previous studies, both UV emission and green-band emission (G-band) are observed at 3.21 eV and 2.50 eV, respectively [3]. The intensity ratio (UV emission / G-band) increases as growth temperature increase. The increase of the absolute PL intensity does not simply mean the excellence of optical property. Generally, not the absolute PL intensity but the relative intensity ratio of I_{UV} to $I_{G\text{-}band}$ is connected to the crystal quality of nanostructures [3]. The UV emission at 3.21 eV is assigned to near band edge emission of ZnO. While, the origin of G-band is believed to be related with the native defects such as Zn interstitial (I_{Zn}) [20-21], Zn vacancy (V_{Zn}) [36], and oxygen vacancy (V_O) [36]. In our experiment, as the substrate temperature decrease the density and size of clusters increase, and the clusters are revealed to have a lot of oxygen deficiencies from EDX measurements. Therefore, it is assumed that the increase

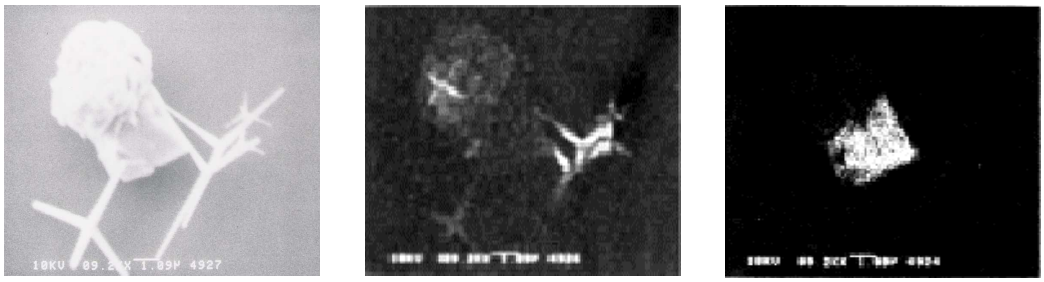

(a) (b) (c)

Fig. 4.4 Comparison of SEM and CL images measured at room temperature. (a) SEM image of ZnO tetrapods and clusters. (b) CL image of ZnO tetrapods recorded at 3.2 eV (c) CL image of ZnO clusters recorded at 2.5 eV. UV emission is dominated from the tetrapods, while green emission is mainly observed from the clusters.

of G-band intensity is closely related with the increase of the density of cluster.

Fig. 4.4 shows CL images measured at room temperature. Fig. 4.4 (a) is a SEM image, which shows several tetrapods along with cluster. While, fig. 4.4 (b) and 4.4 (c) are the CL images, which are recorded by collecting the luminescence at 3.2 eV and 2.5 eV, respectively. As one can see, UV emission is dominated from the tetrapods, however green emission is mainly observed from the clusters. Also the clusters are found to have weak luminescence intensity in compare to the tetrapods that can be explained in terms of the poor crystal quality of clusters due to high defect density.

4.7) Summary

Tetrapod-shape ZnO nanostructures are grown on Si substrates by using vapor phase transport method without any catalyst. High-density tetrapods along with clusters are formed at elevating temperatures. Tetrapods show uniform shape along with almost stoichiometric composition. However, the size and density of clusters show close correlation to the growth temperature, also the clusters are revealed to have a lot of oxygen deficiencies. It is discussed that the oxygen deficiencies are originated from the segregation of liquid phase Zn and Zn-suboxides, which are responsible for the green emission.

References

[1] Z.K. Tang, G. K, L. Wang, P. Yu et al, Appl. Phys. Lett. 72 3270 (1998)

[2] K. Park, J.S. Lee, M.Y. Sung et al, J. Appl. Phys. 41 7317 (2002)

[3] B.D. Yao, Y.F. Chen, N. Wang, Appl. Phys. Lett. 81 757 (2002)

[4] Z. Chen, N. Wu, Z. Shan, S.X. Mao et al, Scripta Mater. 52 63 (2005)

[5] J.H. Choy, E.S. Jang, J.H. Won et al, Appl. Phys. Lett. 84 282 (2004)

[6] S. R. C. Vivekchand, G. Gundiah et al, Adv. Mater. 16 1842 (2004)

[7] C.J. Lee, T.J. Lee et al, Appl. Phys. Lett. 81 3648 (2002)

[8] Q.X. Zhao, M. Willander et al, Appl. Phys. Lett. 83 165 (2003)

[9] M. Izaki , S. Watase , H. Takahashi , Adv. Mater. 15 2000 (2003)

[10] M.H. Huang, Y. Wu, H. Feick et al, Adv. Mater. 13 113 (2001)

[11] H. T. Ng, J. Li, M. K. Smith et al, Science 300, 1249 (2003)

[12] S. Y. Li, C. Y. Lee, and T. Y. Tseng, J. Cryst. Growth 247 357 (2003)

[13] S.C. Lyu, Y. Zhang, H. Ruh et al, Chem. Phys. Lett. 363 134 (2002)

[14] W.D. Yu, X.M. Li, X.D. Gao, Appl. Phys. Lett. 84 2658 (2004)

[15] W.I. Park, D.H. Kim, S.W. Jung, G.C. Yi, Appl. Phys. Lett. 80 4232 (2002)

[16] T.W. Kim, T. Kawazoe, T. Sekiguchi et al, Appl. Phys. Lett. 84 3358 (2004)

[17] Q. Wan, K. Yu, T.H. Wang, C.L. Lin, Appl. Phys. Lett. 83 2253 (2003)

[18] Y.B. Li, Y. Bando, T. Sato et al, Appl. Phys. Lett. 81 144 (2002)

[19] L. Dloczik, R. Engelhardt, K. Ernst et al, Appl. Phys. Lett. 78 3687 (2001)

[20] J.Q. Hu, Y. Bando, J.H. Zhan et al, Appl. Phys. Lett. 83 4414 (2003)

[21] V.A.L. Roy, A.B. Djurisic, W.K. Chan et al, Appl. Phys. Lett. 83 141 (2003)

[22] H. Yan, R. He, J. Pham, P. Yang , Adv. Mater. 15 402 (2003)

[23] Q.H. Li, Q. Wan, Y.J. Chen et al, Appl. Phys. Lett. 85 636 (2004)

[24] B.K. Meyer, H. Alves, D.M. Hoffmann et al, Phys. Stat. Sol. B 241 231 (2004)

[25] D.C. Look, C. Coskun, B. Claflin et al, Physica B 340-342 32 (2003)

[26] U. Ozgur, Y.I. Alivov, C. Liu et al, J. Appl. Phys. 98 041301 (2005)

[27] D.C. Look, R.L. Jones et al, Phys. Stat. Sol. A 195 171 (2003)

[28] A. Take, U. Ozgur, S. Dogan et al, Phys.Rev. B 70 195207 (2004)

[29] H.J. Ko, Y. Chen, Z. Zhu et al, J. Cryst. Growth 77 537 (2000)

[30] D. Li, Y.H. Leung, A.B. Djurisic et al, Appl. Phys. Lett. 85 1601 (2004)

[31] H.J. Fan, R. Scholz, F.M. Kolb et al, Appl. Phys. Lett. 79 1895 (2004)

[32] T. Yashi, M. Yasuda, D. Nezaki et al, Thin Solid films 464-465 273 (2004)

[33] Y.H. Leung, A.B. Djurisic, J. Gao et al, Chem. Phys. Lett. 385 155 (2004)

[34] Binary alloy phase diagrams, 2nd edition, edited by Thaddeus B. Massalski, materials park, 1990 Vol. 3, p2938

[35] Y. Dai, Y. Zhang, Q.K. Li et al, Chem. Phys. Lett. 83 358 (2002)

[36] R.C. Wang, C.P. Liu, J.L, Huang et al, Appl. Phys. Lett. 86 251104 (2005)

[37] M. Kitano, T. Hamabe et al, J. Cryst. Growth 102 965 (1990)

Chapter 5. Applications of high-quality ZnO nano-tetrapods

5.1) Introduction

ZnO is a semiconductor with a wide direct band gap of 3.44 eV (4 K) and a large exciton binding energy of 60 meV. Therefore, the ZnO-based nanostructures are known to be attractive candidates for many application fields. Recently, numerous studies have been performed on various ZnO nanostructures [1-7]. ZnO nanostructures have been regarded as an appropriate alternative to carbon nanotubes (CNTs) for field emission devices due to their high mechanical strength, thermal stability, and ambient insensitivity. Already, there have been several reports on the successful demonstration of high-performance field emitters [4, 8] using ZnO nanostructures. Among the diverse ZnO nanostructures, tetrapod-shaped nanostructures are known to be one of most suitable structures for field-emitter applications, and the best is almost comparable to that of CNTs [9-11].

Since the demonstration of the ultraviolet lasing emission from ZnO nanowires [14] is realized, nanostructured ZnO has been regarded as the attracting material for blue optoelectronic applications. To achieve efficient excitonic laser action at room temperature, the binding energy of the exciton

must be much greater than the thermal energy at room temperature (26 meV). As previously stated, ZnO is a good candidate because its exciton binding energy is ~ 60 meV, substantially larger than that of ZnSe (22 meV) and GaN (25 meV).

In this chapter, ZnO tetrapod structures, which was shown the best high-quality properties in the 3 chapter, were applied to the demonstration of a low-threshold-voltage field emitter and optically pumped lasing.

5.2) Previous studies

5.2.1) Field emission properties of ZnO nanostructures

CNTs have been widely investigated for field emission (FE) for years. However, besides the geometric factors, thermal stability, and ambient insensitivity are equally important to the operation of field emitters [12]. As an oxide, ZnO exhibits high melting point (1975 ^{o}C) and large exciton binding energy (~60 meV) [13], which makes it have more thermal stability and ambient insensitivity compared with CNTs. In addition, ZnO is more resistant is radiation and oxidation, which is essential to the application of FE.

5.2.2) Current-Voltage measurements

Usually current-voltage (I-V) measurements are used to characterize the electron emission behavior according to the Fowler-Nordheim (FN) relation.

Form these measurements technologically important parameters such as threshold field F_{th} or the current density J can be determined, but not work function ϕ as the physically relevant parameter. The reason for this is that experimentally one does not measure current-field characteristics but current-voltage characteristics, where one relates the applied voltage to some applied field for example by dividing the applied voltage with the anode cathode distance.

In order to understand the emission behavior, I-V data are also analyzed by applying the Fowler-Nordheim (FN) equation:

$$J = \frac{aV^2}{\beta^2 d^2 \phi} \exp\left(\frac{bd\phi^{3/2}}{\beta V}\right)$$

where J is the current density [Am^{-2}], V is the applied voltage [V], ϕ is the work function [eV], β is the field enhancement factor, and $z=1.56 \times 10^{-10}$ $AeVV^{-2}$ and $b=6.83 \times 10^{-10}$ $Vm^{-1}eV^{-3/2}$. The FN emission behavior can be examined from the linearity of curves by plotting ln (I/V^2) versus 1/V. The slope of this straight line will be equal to

$$VN_{slope} = -A_v \frac{\phi^{1.5}}{\beta}$$

V is a function of the applied voltage, whereas β generally is unknown. In case of well-defined emitter geometry the work function ϕ can be calculated within certain accuracy. In case of thin film emitters this is generally not possible. This means that the work function ϕ of the emitter cannot be determined from the

measurement of the I-V characteristics alone.

5.2.3) Basic principles on the stimulated emission

Due to its high exciton-binding energy, ZnO is of interest for the achievement of excitonic stimulated emission at room temperature, which has a lower threshold than electron-hole plasma recombination. While, there have been numerous reports on optically pumped lasing and amplified spontaneous emission from ZnO [14], no electrically pumped lasing has been achieved as yet. Lasing has been reported in a number of different structures such as, nanowires [15], tetrapods [16], and nanoribbons/combs [17]. A very broad range of lasing thresholds has been reported for different ZnO nanostructures, ranging form 8 $kWcm^{-2}$ (ZnO fibers) [18] to 867 $kWcm^{-2}$ (ZnO nanorods) [19].

Stimulated emission in ZnO can be achieved either by exciton-exciton scattering (EES) or electron-hole plasma (EHP) recombination. As the excitation power increases, sharp peaks will appear in the emission spectra. Due to the significantly shorter decay time of the stimulated emission compared to spontaneous emission, lasing peaks can be observed more clearly in time-resolved spectra. As the excitation power increases, the increase in intensity and the appearance of narrow lasing modes can be observed. With a further increase of excitation power, lasing in the EHP mode occurs.

The peak position of the emission resulting from inelastic collisions

between excitons is given by:

$$E_n = E_{ex} - E_{ex}^b(1-1/n^2) - 3kT/2$$

where n=2,3,…, k is the Boltzmann constant, T is the temperature, and E_{ex}^b=60 meV is the exciton binding energy. The transition from spontaneous emission to stimulated emission is evidenced by narrowing of the emission with a full-width half maximum (FWHM) about two orders of magnitude lower compared to the FWHM of spontaneous emission. The threshold for lasing due to exciton-exciton scattering in nanostructure is typically 2-3 times lower than that for lasing in the EHP regime.

With increasing excitation energy, the density of the excitons in ZnO will also increase. As the exciton density increases, binding energy decreases. The EHP plasma forms at densities higher than the “Mott density” given by [13]:

$$n_M = \frac{kT}{2a_B^3 E_{ex}^b}$$

where a_B is the Bohr radius. The Mott density is estimated to be ≈ 3.7 x 10^{19} cm^{-3} [13], although lower estimated such as ≈ 4 x $10^{18}$$cm^{-3}$ have also been reported [20]. The EHP emission is typically more broad and red shifted compared to emission due to exciton-exciton scattering [13]. The red shift of the EHP emission is the result of bandgap renormalization.

5.2.4) Nanostructures as fabry-perot resonators

Detailed mode analysis of nanostructures as laser cavities has been performed [20-21]. Good agreement in ZnO nanowires between the measured modes with similar polarization and expected mode spacing is given by:

$$\Delta\lambda = \frac{\lambda^2}{2L\left(n - \lambda\frac{dn}{d\lambda}\right)}$$

where $\Delta\lambda$ is the mode spacing, λ is the wavelength, n is the refractive index, and L is the length. The linewidth of the measured lasing modes was also in good agreement form the theoretical estimate of the order of 1 nm obtained for a Fabry-Perot resonator by using the following expression [20]:

$$\Delta\nu = -\frac{c}{4\pi Ln}\ln[R_1R_2(1-T_i)^2]$$

where c is the speed of light, R_1 and R_2 are the reflectivities of the mirrors, and T_i is the transmittance of the internal medium of the cavity. The threshold gain can be expressed as [22]:

$$g_{th} = \alpha + \frac{1}{2L}\ln^{-1}(R_1R_2)$$

where L is the length and α is the absorption loss. It should be noted, however, that thresholds in individual nanowires differences in dimensions, the condition of the cavity, and the extent of substrate coupling [20].

Among other more complicated cavities, ZnO tetrapods have been most

thoroughly studies. The each leg of the tetrapod acts as an individual laser [16]. The lasing from multiple tetrapod arms occurs only if all the arms are excited, otherwise lasing will occur only from the excited are due to high losses in the non-excited tetrapod arms [23].

5.3) Experimental

Field-emission measurements with grown high-quality ZnO tetrapod in optimum growth condition were performed in a vacuum chamber at a pressure of $< 1 \times 10^{-5}$ Torr at room temperature. The distance between the two electrodes was estimated as ~ 950 μm, and the measured emission area was 4 mm^2. The emission current was measured by applying voltages up to 1000 V.

Photoluminescence spectra of ZnO tetrapod structure were measured with a He-Cd laser (325 nm) as an excitation source. In order to explore the possible stimulated emission from the high-quality ZnO tetrapods, the power-dependent emission has been examined. The sample was optically pumped by Nd:YAG (Yttrium-Aluminum-Garnet) laser (355 nm, 5ns) at room temperature.

5.4) Field emitter realization of ZnO nanotetrapods

Figure 5.1 illustrates the emission current density from ZnO tetrapods grown on Si substrate, as shown in Fig. 3.1 (c). The inset is the device configuration. The turn-on voltage is estimated to be about 1 V/μm at a current

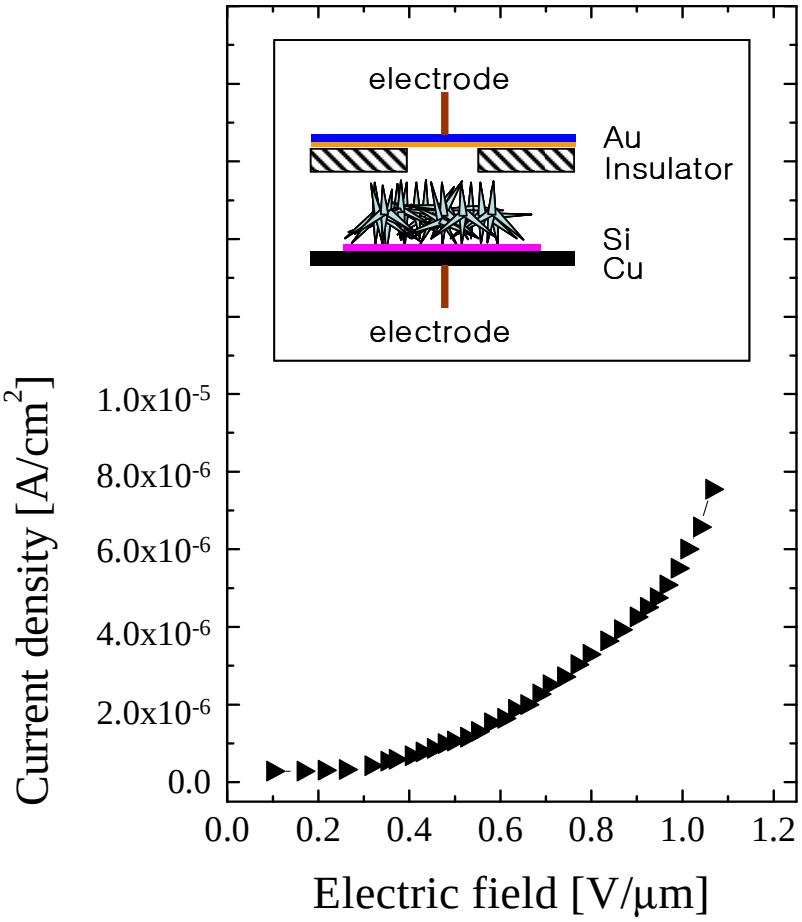

Fig. 5.1 Field emission characteristics of the ZnO tetrapod field emitter; The turn-on voltage is about 1 V/μm at a current density of 6 μA/cm^2. The inset is a schematic drawing of the device configuration.

density of 6 μA/cm^2. Note that the reported lowest turn-on field from tetrapod structures is 1.6 V/μm at a current density of 1 μA/cm^2 [4, 12, 24]. The field emission property is deeply related to the geometry, the structure and the density of the nanostructures [24-26]. The low emission field should be attributed to the high structural quality of the tetrapod structures.

5.5) Optical pumped lasing at room temperature of the ZnO nanotetrapods

Fig. 5.2 shows the luminescence spectrum excited at low excitation intensity with a CW He-Cd laser (325 nm) as an excitation source, which is indicated on the down position in black line. And other spectra are measured by using Nd:YAG (355 nm, 5 ns) under different excitation intensities at room

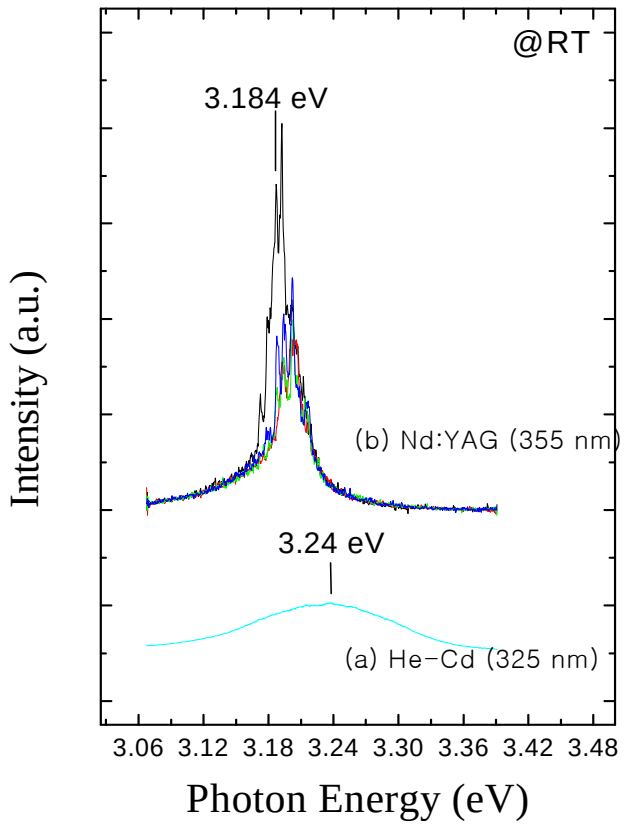

Fig. 5.2 (a) The PL spectra excited by the 325 nm line of a CW He-Cd laser. Stimulated emission spectrum as a function of the pumping intensity provided by the Nd:YAG laser (355 nm 5ns).

temperature.

At low excitation intensity, the spectrum consists of a single broad spontaneous emission with a full width at half maximum of ~ 140 meV. The corresponding emission mechanism is related to the near-band-edge radiative recombination such as free exciton (~3. 26 eV), exciton-exciton scattering (EES, ~3.18 eV), and electron-hole plasma (EHP ~3.14 eV) recombination. As shown in fig. 5.2 (a), the spontaneous emission centered at 3.24 eV, which is 130 meV below the band gap (3.37 eV), is generally ascribed to the recombination of free exciton (FX).

As the pump power increases in the fig 5.2 (b), the emission peaks narrow because of the preferential amplification of frequencies close to the maximum of the gain spectrum. With the excitation intensity increasing, the spontaneous free exciton emission (FX) is gradually replaced by a new band labeled P-band (3.184 eV) that is located at 56 meV below the FX band. The P-band is commonly shown as resulting of exciton-excitons scattering [14].

The linewidth of these narrow peaks is about 1 nm. By using the equation between mode spacing and cavity length in the section 5.2.4), we could obtain that the cavity length is estimated to be 30 μm. However, note that the length of the real ZnO nanotetrapod is 1 μm. Therefore the lasing mechanism is regarded as not a conventional lasing but the random lasing. The random lasing in ZnO was reported in polycrystalline thin films, nanoparticle,

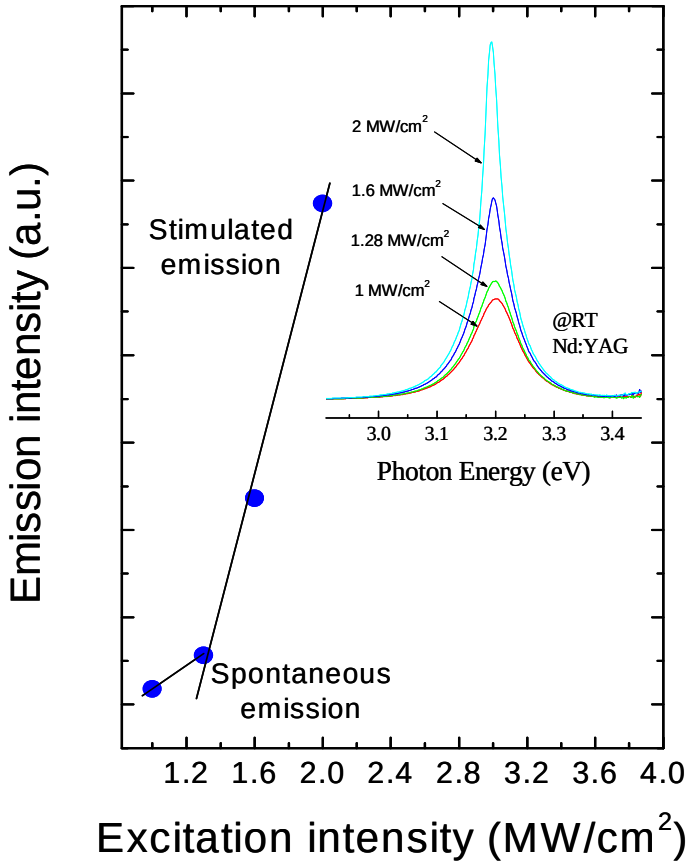

Fig. 5.3 Lasing characteristics of the ZnO tetrapod nanostructure at RT. The threshold intensity for lasing is 1.3 MW cm^{-2} at 355 nm. The inset shows the variation of lasing spectrum with excitation intensity.

nanorods, nanoneedles, and nanowires [14-17]. One distinguishing characteristic of a random laser is that stimulated emission can be observed in all directions. For the case of a nanowire with random lasing, it is difficult to establish from angular-dependence measurements of the emission spectra whether the feedback originates from individual wires acting as resonators or from scattering between wires. Another characteristic of the random laser is that

the lasing threshold depends on the excitation area. The lasing threshold increases as the excitation area decreases.

Fig. 5.3 shows the evolution of lasing emission at 355 nm with increase in optical excitation intensity at room temperature. With the excitation intensity increasing, the threshold intensity for lasing is estimated as 1.3 MW cm^{-2}.

Different lasing mechanisms, lasing wavelengths and lasing thresholds

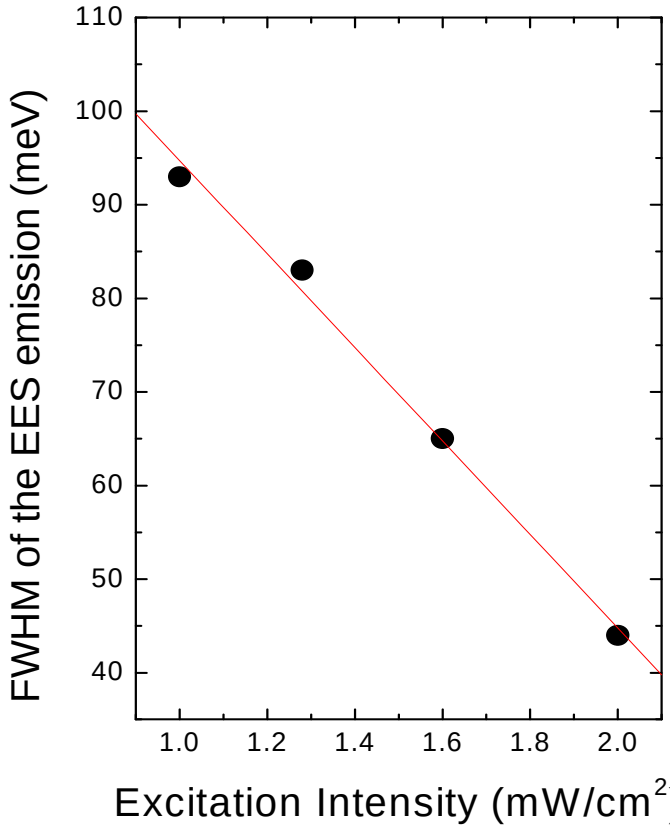

Fig. 5.4 FWHM variation of the P-band (EES) dependence of the excitation intensity

have been reported from the various ZnO nanostructures. The variation in the lasing threshold is expected even for individual nanostructures with the same morphology, due to differences in their dimensions and other properties [14-17]. The high threshold excitation intensity might be come from the lasing by random cavity. Although, in general, lasing by an exciton-exciton scattering mechanism shows lower threshold intensity, formation of a random cavity indicates increase of external loss.

Fig. 5.4 shows FHWM change of the P-band (EES) obtained under different excitation levels. With excitation intensity increasing, a linewidth decreases from 93 meV to 43 meV. It is due to the luminescence mechanism transition from spontaneous emission to stimulated emission.

5.6) Conclusions

We have investigated the feasibility of the tetrapod ZnO nanostructure. From the field emission experiment, a low turn-on voltage of 1 V/μm operation is achieved. It has been demonstrated to be suitable for applications as high-performance field emitters. As well as, the ultraviolet lasing of ZnO tetrapod has been realized at room temperature. The lasing mechanism is discussed in terms of exciton-exciton scattering and the formation of random cavity is attributed to responsible for the high threshold intensity.

References

[1] W. D. Yu, X. M. Li, and X.D. Gao, Appl. Phys. Lett. 84 2658 (2004)

[2] W. I. Park, D. H. Kim, S-W. Jung, and G. C. Yi, Appl. Phys. Lett. 80 4232 (2002)

[3] T. W. Kim, T. Kawazoe, S. Yamazaki, M. Ohtsu, and T. Sekiguchi, Appl. Phys. Lett. 84 3358 (2004)

[4] Q. Wan, K. Yu, T. H. Wang, and C. L. Lin, Appl. Phys. Lett. 83 2253 (2003)

[5] Y. B. Li, Y. Bando, T. Sato, and K. Kurashima, Appl. Phys. Lett. 81 144 (2002)

[6] L. Dloczik, R. Engelhardt, K. Ernst, S. Fiechter, I. Sieber, and R. Konenkamp, Appl. Phys. Lett. 78 3687 (2001)

[7] W. I. Park, J. Yoo, and G. C. Yi, J. Korean. Phys. Soc. 46 1067 (2005)

[8] Y. H. Leung, A. B. Djurisic, J. Gao, M. H. Xie, and W. K. Chan, Chem. Phys. Lett. 385 155 (2004)

[9] W. Zhu, C. Bower, O. Zhou, G. Kochanski, and S. Jin, Appl. Phys. Lett. 75 873 (1999)

[10] C. J. Lee, J. Park, S. Y. Kang, and J. H. Lee, Chem. Phys. Lett. 326 175 (2000)

[11] S. H. Jeong and K. H. Lee, J. Korean. Phys. Soc. 45 252 (2004)

[12] C.J. Lee, T.J. Lee, S.C. Lyu et al. Appl. Phys. Lett. 81 3648 (2002)

[13] U. Ozgur, Y.I. Alivov, C. Liu et al, J. Appl. Phys. 98 041301 (2005)

[14] M.H. Huang, S. Mao, H. Feick et al, Science 292 1897 (2001)

[15] M.H. Huang, Y. Wu, H. Feick et al, Adv. Mater. 13 113 (2001)

[16] J.M. Sarko, J.K. Song et al, Chem. Phys. Lett. 404 171 (2005)

[17] A.B. Djurisic, W.M. Kwok, Y. H. Leung et al, J. Phys. Chem. B 109 19228 (2005)

[18] J-H. Choy, E-S. Jang et al, Appl. Phys. Lett. 84 287 (2004)

[19] X. Han, G. Wang, Q. Wang et al, Appl. Phys. Lett. 86 223106 (2005)

[20] J.C. Johnson, H. Yan, P. Yang et al, J. Phys. Chem. B 107 8816 (2003)

[21] D.J. Sirbuly, M. Law et al, J. Phys. Chem. B 109 15190 (2005)

[22] H. Yan, J. Johnson, M. Law et al, Adv. Mater. 15 1907 (2003)

[23] J.K. Song, J.H. Szarko, S.R. Leone et al, J. Phys. Chem. B 109 15749 (2005)

[24] Q. Zhao, H. Z. Zhang, Y. W. Zhu, S. Q. Feng, X. C. Sun, J. Xu, and D. P. Yu, Appl. Phys. Lett. 86, 203115 (2005)

[25] C. C. Chang and C. S. Chang, Solid State Commun. 135, 765 (2005)

[26] D.H. Kim and H.R. Lee, J. Korean. Phys. Soc. 45, 248 (2004)

Chapter 6. Summary and conclusions

A widely accepted definition of a nanostructure is a system in which at least one-dimension is ≤100 nm, typically including layer-type, wire-type, and particle-type structures. Quantum effects due to size confinement in nanostructures occur when the characteristic size of the object is comparable with the critical lengths (typically 1-10 nm) of the corresponding physical processes, such as the mean free path of electrons, the coherence length, or the screening length.

Oxides are the basis of smart and functional materials. Synthesis and device fabrication using functional oxides have attracted a lot of attention recently because the physical properties of these oxides can be tuned. Among them, II-VI semiconductor compound ZnO is considered to be the most prospective one due to its large exciton binding energy (60 meV), high electromechanical coupling constant, and resistivity to harsh environment. And when it is fabricated to the nanostructure, there are promising potentials in extensive applications such as nanolaser, nanocantilevers, field emitters (FEs), and nano gas sensor. Therefore, ZnO nanostructures stimulated so much attention, and a large number of publications have appeared lately reporting nanostructures of various shapes grown by different methods.

In this thesis, it has focused on the synthesis, characterization, and

application of ZnO nanostructure. In the chapter 1, it is exhibited the basic ZnO properties, characteristics in the nanostructure, and applications for the many semiconductor devices. In the chapter 2, the principles of analysis measurements, scanning electron microscope (SEM), energy dispersive x-ray spectroscope (EDX), cathodoluminescence (CL), and photoluminescence (PL), to estimate of the synthesized ZnO nanostructures are described. In the chapter 3, the shape of various ZnO nanostructures (cluster, wire-type, tetrapod-type) is controlled by the change of VI/II supplying ratio with systematically adjusting growth conditions such as growth temperature and carrier gas flux. The feasibility of the uniform ZnO nanotetrapods grown at the optimum growth condition for a practical application is tested in the chapter 5. In the chapter 4, mainly the luminescence properties of ZnO nanostructure are elucidated. It has proved that the green emission is originated from clusters with oxygen deficiency. And the luminescence mechanisms of UV emission have been investigated from the low-temperature photoluminescence (LT-PL) measurements.

In the chapter 5, feasibilities of ZnO nanostructures for many applications are confirmed by field emitter device test and optically pumping experiment at room temperature.

감사의 글

본 논문을 마무리하며 그 동안의 석사 생활 동안 감사했던 분들을 다시 한번 되새겨 봅니다. 많은 도움을 주신 분들이 계셨기에 2년 동안의 생활이 더 값지고 의미가 있었던 것 같습니다. 처음 연구실에 들어오겠다는 저를 믿어주시고 끊임없는 인내력으로 보살펴 주시며 지도해 주신 장지호 교수님께 진심 어린 감사의 마음을 전합니다. 항상 연구실의 발전을 위해 노력하시고 진심으로 학생들을 지도해 주시는 모습을 통해 많은 것을 배우고 따르려고 합니다. 그리고 많은 조언을 해 주셨던 이삼넝 교수님, 안형수 교수님, 양민 교수님, 김홍승 교수님께도 감사하다는 말씀을 드리고 싶습니다. 또한 이홍찬 교수님, 고항주 박사님, 오동철 교수님, 김정진 박사님의 많은 조언에 감사했습니다.

항상 너그럽고 친절하신 이봉춘 조교님, 김경화 선배님, 이정윤 선배님, 이주영 선배님과 이호준 선배님, 그리고 재현이.. 감사의 마음을 표합니다. 같은 석사 동기생인 대현오빠, 명훈 오빠, 근숙이, 은수에게도 고맙다는 인사를 전합니다. 항상 후배들을 챙겨주시고 노력하시는 박승환 선배님, 성실하고 열심히 하는 후배 선여, 연구실의 가장 든든하고 유쾌한 웅 오빠, 규범이 오빠, 광희 오빠, 진우 오빠, 현경이, 성국이 오빠, 상훈이, 시영이, 승준이.. 많은 사람들이 연구실을 거쳐 갔고, 지금도 동고동락하며 생활하고 있습니다. 그런 연구실 식구들께 항상 고맙고 함께이기에 든든한 마음은 달리 표현할 방법이 없다고 생각합니다.

그리고 석사 과정 중 짧지만 길었던 6 개월의 일본 생활 동안 챙겨주시고 보

살펴 주신 분들께도 감사하다는 말씀을 올립니다. 저의 지도 교수님의 은사님이신 동북대학교 야오 연구실 Takafumi Yao 선생님께 감사하다는 말씀을 드립니다. 그리고 측정해 주신다고 고생하시고 많은 조언을 주신 Takenori Goto 선생님과 무라카미 상께도 감사하다는 말씀을 전합니다. Hanada 선생님, 조명환 박사님, 임인호 박사님과 사모님, 진섭이 오빠와 언니, 이석우 씨와 언니, 이욱현 씨, 상현 오빠와 현정이 언니, 그 외 많은 한국 분들.. 그 분들이 보살펴 주시고 걱정해 주신 덕분에 6 개월 동안의 생활이 외롭지 않고 든든했었습니다. 감사하다는 말씀을 전합니다. 또한 아주 따뜻하고 친절했던 엔도 상 아주머니, 덕분에 마음 편히 지낼 수 있었고, 자라 상, 미네기시 상, 고토 상, 가토 상, 고바야시 상, Lyon으로부터 받은 많은 도움과 조언에 다시금 감사의 마음을 전합니다. 그 밖에 도와주신 많은 분들께 감사하다는 말씀을 꼭 전하고 싶습니다. 바쁘다는 핑계로 자주 얼굴도 보지 못하지만 그래도 자주 안부를 물어주었던 철휴, 영희, 미주, 선주, 현이,, 항상 미안한 마음이 가슴 한 켠에 있는 소중한 저의 친구들과도 인사를 나누고 싶습니다.

그리고 마지막으로 하나 밖에 없는 언니와 형부, 저의 가장 든든한 지원군이신 부모님께 정말 감사하다는 말씀을 전해 드립니다. 철부지 막내딸의 의사를 항상 존중해 주시고 믿어주시는 부모님께 한 없이 죄송하고 미안하지만 그 분들이 항상 제 곁에 계셔주기에 제가 존재하는 것 같습니다. 항상 사랑하고 존경합니다. 더 생각하고 열심히 하고 자만하지 않는 사람이 되도록 노력하겠습니다.